



Article

Do We Need a Higher Resolution? Case Study: Sentinel-1-Based Change Detection of the 2018 Hokkaido Landslides, Japan

István Péter Kovács ¹, Giulia Tessari ², Fumitaka Ogushi ³, Paolo Riccardi ², Levente Ronczyk ¹,
Dániel Márton Kovács ^{4,*}, Dénes Lóczy ⁵ and Paolo Pasquali ²

¹ Department of Cartography and Geoinformatics, University of Pécs, 7624 Pécs, Hungary; vonbock@gamma.ttk.pte.hu (I.P.K.); hidrogen@gamma.ttk.pte.hu (L.R.)

² Sarmap SA, 6987 Caslano, Switzerland; gtessari@sarmap.ch (G.T.); paolino@sarmap.ch (P.R.); ppasquali@sarmap.ch (P.P.)

³ L3 Harris Geospatial, Tokyo 113-0033, Japan; fumitaka.ogushi@l3harris.com

⁴ Doctoral School of Earth Sciences, University of Pécs, 7624 Pécs, Hungary

⁵ Department of Physical and Environmental Geography, University of Pécs, 7624 Pécs, Hungary; loczyd@gamma.ttk.pte.hu

* Correspondence: kdanielm@gamma.ttk.pte.hu



Citation: Kovács, I.P.; Tessari, G.; Ogushi, F.; Riccardi, P.; Ronczyk, L.; Kovács, D.M.; Lóczy, D.; Pasquali, P. Do We Need a Higher Resolution? Case Study: Sentinel-1-Based Change Detection of the 2018 Hokkaido Landslides, Japan. *Remote Sens.* **2022**, *14*, 1350. <https://doi.org/10.3390/rs14061350>

Academic Editors: Bruno Adriano, Sadra Karimzadeh, Luis Moya, Bahareh Kalantar, Alok Bhardwaj and Yanbing Bai

Received: 29 January 2022

Accepted: 8 March 2022

Published: 10 March 2022

Publisher's Note: MDPI stays neutral with regard to jurisdictional claims in published maps and institutional affiliations.



Copyright: © 2022 by the authors. Licensee MDPI, Basel, Switzerland. This article is an open access article distributed under the terms and conditions of the Creative Commons Attribution (CC BY) license (<https://creativecommons.org/licenses/by/4.0/>).

Abstract: Since 2014, Sentinel-1 (S1) Synthetic Aperture Radar (SAR) data have become an important source in the field of displacement detection thanks to regular acquisitions and 7.5 years of temporal coverage at global level. Despite the increasing number of publications on the role of S1 in landslide detection, there is still a need for research to further clarify the capabilities of the sensor and the applicable image analysis techniques. Previous studies have successfully exploited high-resolution ALOS-PALSAR image-based intensity and coherence analysis at the 2018 Hokkaido landslides. Nevertheless, they expressed a clear need to analyse the capabilities of other sensors (such as S1). This raises the question: Do we need SAR imagery with higher spatial resolution (such as ALOS-PALSAR) or are freely available S1 imagery also suitable for rapid landslide detection? The S1 images could provide suitable material for a comparative analysis and could answer the aforementioned question. Therefore, 17 ascending and 19 descending S1 images were analysed to test S1 accuracy on landslide detection. Multitemporal analyses of both intensity and coherence were performed along with coherence differences, multitemporal features (MTF) and MTF differences of coherence images. In addition, the spatial analysis of the classification results was also evaluated to highlight the potential of S1 coherence analysis. S1 was found to have limitations at the site, as single coherence differences provided low-quality results. However, the results were significantly improved by calculating the MTF on coherence and almost reached the success rate of the ALOS-PALSAR-based coherence analysis, even though the improvement of the results with intensity was not possible. Half of the false positives were identified in the 30–45-m buffer zone of the agreement, underlining that the spatial resolution of the S1 is not appropriate for accurate landslide detection. Only an approximation of the landslide-affected area can be given with considerable overestimation. Due to the inclusion of post-event images, the sensor is not perfectly applicable for rapid detection purposes here.

Keywords: Sentinel-1; landslide mapping; change detection; coherence; intensity; multi-temporal features

1. Introduction

Due to intense population growth, urbanisation, economic development and climate change, landslides have become the most hazardous surface processes, causing economic and human losses worldwide [1–6]. Therefore, landslide detection and analysis has become one of the most important research topics in geosciences. The number of papers focusing

on landslide mapping, monitoring and prediction is rapidly rising [7], and it is essential to further refine landslide toolboxes.

To best match their needs, researchers can choose from dozens of landslide mapping and monitoring techniques [8–10]. Most common ground-based techniques, such as field geodesy, including total station or levelling-based monitoring networks [11,12], inclinometer and extensometer surveys [13], GPS (Global Positioning System) surveys [14], geomorphological mapping [15] and TLS (Terrestrial Laser Scanning) [16] and GB-InSAR (Ground-based Synthetic Aperture Radar Interferometry) [17], require more effort for on-site measurements [18,19] and provide high-resolution, detailed data, but only for a limited area [20–22]. Remote sensing techniques, such as orthophoto interpretation, photogrammetry, LIDAR [23], InSAR (Synthetic Aperture Radar Interferometry), DInSAR (Differential Synthetic Aperture Radar Interferometry) and interferometric stacking techniques [24–26] on the other hand usually focus on larger areas from a remote location [27,28]. In addition to the resolution, the accuracy and precision of the obtained results may differ according to the applied technique [10,29], but the applicability of the methods may also vary depending on the actual field conditions [30]. Moreover, there are various GIS tools and modelling approaches available for landslide hazard and risk assessment [31–33].

Active SAR satellites have overcome the limitations of passive sensors (e.g., cloud cover that normally obscures surface processes) and provide coherent measurements of the ground surface in different weather and light conditions, even day and night [34]. Therefore, InSAR and DInSAR in particular have become standard tools for landslide detection, mapping and monitoring [24]. The continuous flow of freely available data from the European Space Agency's (ESA) Copernicus Programme has significantly increased the number of published papers since the launch of S1 in 2014 [35–39]. Despite the ability of SAR sensors to collect data in all weather conditions, during day and night, atmospheric processes still affect the detection of surface deformations [17]. By processing dozens of SAR images from the same site while evaluating various advanced interferometric stacking techniques such as permanent scatterers (PS), persistent scatterers (PSI), Small-Baseline Subsets (SBAS) or others [28,40–44], it is possible to eliminate the effect of atmospheric artefacts from measurements applying an Atmospheric Phase Screen (APS). Thus, the accuracy of the detection of surface movements can reach a few mm/year (highly depending on the wavelength of the applied sensor), while DInSAR measures, which are based on usually one image pair, are far more inaccurate (cm-scale accuracy). However, stacking techniques can only detect slow or extremely slow-moving landslides, where the displacements do not exceed a quarter of the wavelength between subsequent acquisitions. If fast surface changes cannot be detected with stacking tools, how can we survey landslides caused by a single event over a larger area?

It should also be noted that the above-mentioned techniques can only be applied to displacements of coherent surfaces (mostly non-vegetated, built-up environments). In addition, surface topography, especially in mountainous regions, has a significant impact on the quality of the images, which is influenced by the imaging geometry and the satellite's angle of view. Foreshortening and shadow effects can significantly reduce the extent of recognisable surfaces [45]. Foreshortening can also lead to significant image distortions in mountainous regions, which can be compensated for with high-quality digital elevation models if they do not reach their extreme case, layover, which cannot be resolved. Surfaces in shadow normally cannot be detected but by using different sensor geometries (ascending and descending paths), they could be completely or at least partially explored.

Interferometric techniques use the phase of the measured signal, which describes the distance between the target and the antenna [46]. However, intensity is another useful component of the signal, indicating the amount of backscatter from the surface. Both SAR amplitude and phase are sensitive to changes in the targets within the resolution cell (changes in the scatterers) [34]. Therefore, two different approaches have been developed to use both phase and intensity information from the SAR imagery, referred to as coherent and non-coherent change detection, respectively [47]. These techniques are often used

to map frequent changes, e.g., detecting phenological changes in vegetation, changes in land cover and forests, crop mapping [48–51], or to map rapid, dramatic changes in areas reshaped by diverse destructive processes, e.g., human activities [52], rapid erosion [53], floods [54], earthquakes [55], typhoons or hurricanes [56], urban destruction in conflict zones [57] and landslides [58].

Authors have developed sophisticated change detection techniques in recent decades [53,59–61], testing the capabilities of almost all available sensors individually [62]. Methods such as phase correlation (coherence) [63], coherence difference, coherence ratio [64], normalised coherence difference [65], coherence change index [66], amplitude differences [67], normalised amplitude differences and backscatter coefficient [68], or intensity correlation coefficient [69] were evaluated separately or combined in various ways [70,71]. According to Matsuoka and Yamazaki [72], coherence is more reliable in identifying small-scale changes, while intensity correlation is more informative for large-scale changes. However, the combination of both signal components often leads to more success in mapping landslides [62].

Interferometric coherence and intensity analysis of the Hokkaido landslides was first performed by Aimati et al. [73] and Fujiwara et al. [74]. The authors successfully exploited pre- and co-event (L-band) ALOS-PALSAR imagery with a 3 m resolution for landslide detection. Jung and Yun [75] studied the same area by evaluating multiple coherence and intensity processing techniques and using multi-temporal ALOS-PALSAR imagery. The same authors pointed out that it is necessary to analyse the capabilities of other sensors (e.g., S1) in the landslide detection of the area.

Since 2014, dense coverage of C-band imagery acquired by S1 has been available almost worldwide for surface deformation monitoring. Regular S1 acquisitions (with a 6-day lag over Europe and with 12 days of temporal separation over Japan) so far provide 7.5 years of temporal coverage for each location, which means continuous monitoring of the Earth's surface. However, we know little about the role S1 can play, especially in detecting abrupt-failure landslides such as the 2018 Hokkaido movements. Our paper is dedicated to answering the following questions: 1. Is it possible to use S1 imagery to detect sudden landslides? 2. What types of features/parameters computed from SAR imagery can effectively describe and map landslides? 3. What are the limitations, advantages and disadvantages of S1 imagery in the case of coherent change detection for landslide mapping? 4. Do we need higher spatial resolution imagery (such as ALOS-PALSAR), or can S1-based change detection techniques produce adequate results? In addition, this article also focuses on identifying and revealing problem areas and sources of error in Sentinel-1 data in the case of landslide mapping.

The remainder of the article is organised as follows. Section 2 begins with an introduction to the study area, then lists the data and algorithms used and describes the image processing and classification methods in detail. Section 3 presents the results, while the discussion and conclusions can be found in Sections 4 and 5, respectively.

2. Material and Methods

2.1. Site Description

In August 2018, Typhoon Jebi caused heavy rainfall in Hokkaido, Japan [76], which softened the topsoil layers. Subsequently, on September 6, a magnitude 6.7 earthquake struck the Iburi-Tobu region. The epicentre of the earthquake was near Tomakomai at a depth of 35 km. It involved 41 confirmed deaths and about 700 casualties, and triggered thousands of coseismic landslides. The Geospatial Information Authority of Japan (GSI) identified approximately 6000 landslide scarps and 1000 interconnected debris deposits in a 400 km² area around Atsuma after the event [77]. We believe that these coseismic landslides triggered by the Iburi-Tobu earthquake could provide an ideal study area to test the detection capabilities of S1 imagery.

Most of the landslides were identified as shallow, planar spoon-shaped landslides [78], and only a few deep-seated, dip-slipping landslides were found on the east side of the

affected area [77]. The long-runout landslides were characterized by exposed, uncovered upper slip surfaces [76], while the landslide tongue (fine sediments mixed with pine trees and other debris) often reached rice fields and filled valley floors [77]. The average extent of each landslide reached about 8200 m² [79], and the cumulative area of landslides was 46.3 km² [76]. The landslide inventory of the event conducted by Wang et al. [79] contains 7837 landslides, and they reported 23–38 million m³ of landslide deposits and a density of 326 movements per square kilometre in the affected area.

Landslides have occurred at an elevation of 100–250 m, mainly on slopes of 15–35° [76]. The bedrock consists of Neogene sedimentary rocks and is covered by ~1.5 m thick layers of pumice and ash derived from the Early Holocene eruption of the Tarumai volcano [80]. According to Yamagishi and Yamazaki [77], the thickness of the surface deposits here is up to 4–5 m. Due to the liquefaction and grain crushing caused by the earthquake, the sliding mass was moved on the Ta-d pumice layer [81] and on underlying paleo soils [76].

Our research area is located in central Hokkaido at the westernmost part of the Hidaka Mountains. The site is confined to the western side of the area affected by landslides during the Hokkaido seismic event (based on satellite image coverage) and extends to 384.72 km² (Figure 1). From a geomorphological perspective, the topography of the area consists of young mountain ranges with a maximum elevation of 535 m a.s.l. and adjacent lowland terraces of the Ishikari Depression [76]. Narrow, dissected mountain ridges dominate the landscape. Narrow, deep valleys and short steep slopes connect them to broad floodplains. The landslide area covers 32 km² within our study area (Figure 1A), representing 65.61% of the total area affected by landslides (triggered by the seismic event).

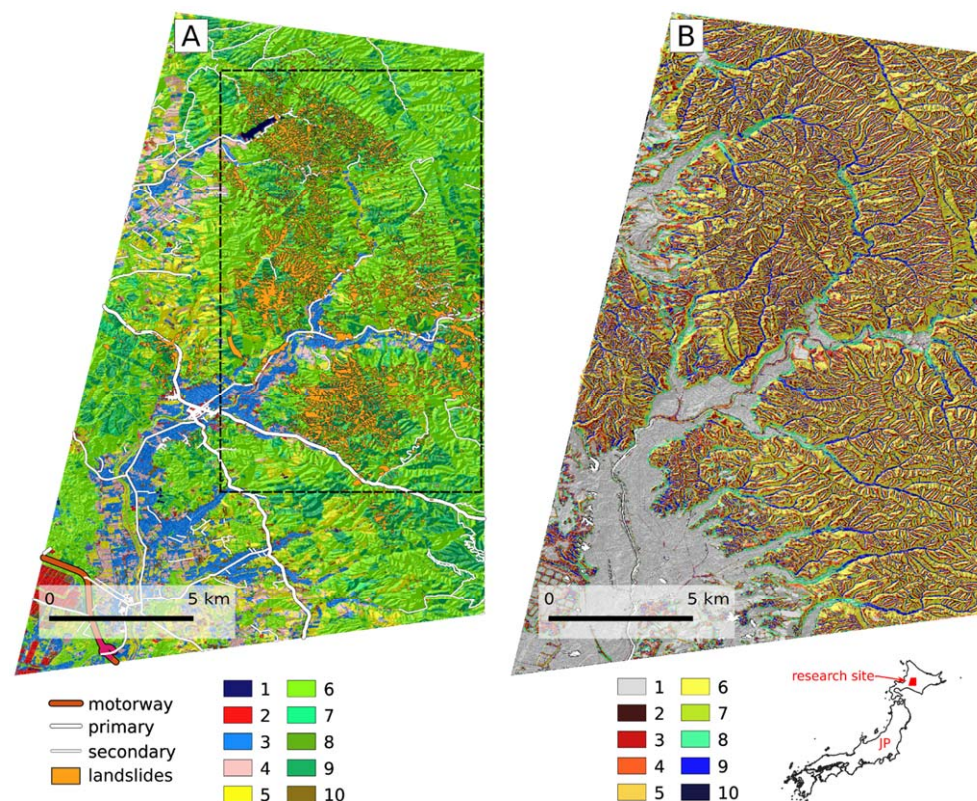


Figure 1. Land use and land cover (A) and terrain forms (B) of the study site. Legend (A): 1 = water; 2 = urban and built-up; 3 = rice paddy; 4 = crops; 5 = grassland; 6 = deciduous broadleaf forest; 7 = deciduous needle-leaf forest; 8 = evergreen broadleaf forest; 9 = evergreen needle-leaf forest; 10 = bare land (data source: HRLULC ver. 16.09 [82]). Dashed line on Figure A indicates the extent of the closer study area. Legend (B): 1 = flat; 2 = summit; 3 = ridge; 4 = shoulder; 5 = spur; 6 = slope; 7 = hollow; 8 = footslope; 9 = valley; 10 = depression. Terrain forms were calculated using the r.geomeorphon module of GRASS GIS and they were named after Jasiewicz and Stepinski [83].

The terrain forms of the entire study area reflect heterogeneity (Figure 1B), with slopes being the predominant terrain types (Figure 2), while ridges, spurs, flat surfaces, and valleys play a roughly equal role in the landscape. The proportions of landforms on which landslides developed, on the other hand, present a different picture. Slopes and valleys were equally dominant, while spurs and hollows played a less important, but still significant part in the developed landslide areas.

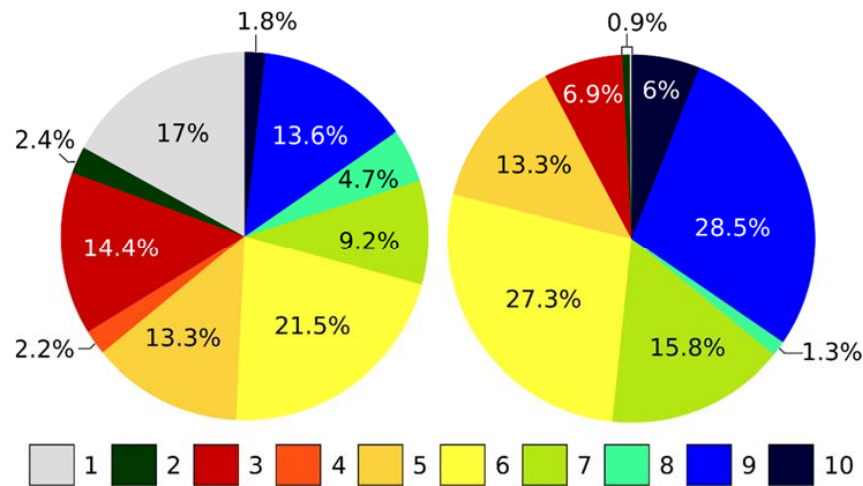


Figure 2. The distribution of terrain forms over the study site (left diagram) and the landslides (right diagram) 1 = flat; 2 = summit; 3 = ridge; 4 = shoulder; 5 = spur; 6 = slope; 7 = hollow; 8 = footslope; 9 = valley; 10 = depression. Terrain forms were calculated and named after Jasiewicz and Stepinski [83].

In terms of vegetation, 91.9% of the landslide area was covered by forest and 7.5% by rice paddies, crops, and grasslands before the event (Figure 3). The land cover of the entire pre-event site reflected different proportions of land use/land cover (LULC) categories, with forests occupying 71.8% of the whole site and rice paddies, crops, and grasslands another 25%.

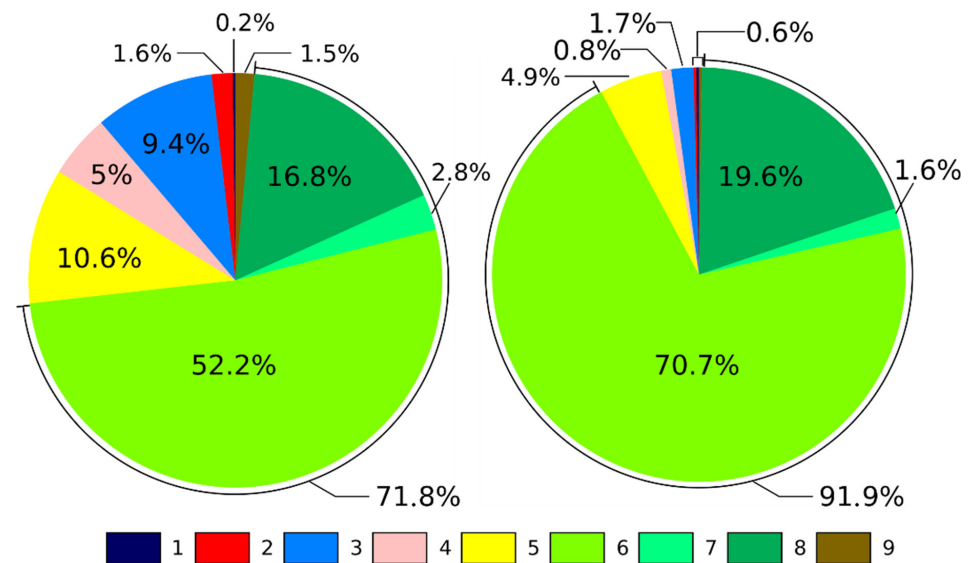


Figure 3. Land use and land cover (LULC) of the research site (left diagram) and the landslides (right diagram). 1 = water; 2 = urban and built-up; 3 = rice paddy; 4 = crops; 5 = grassland; 6 = deciduous broadleaf forest; 7 = deciduous needle-leaf forest; 8 = evergreen broadleaf forest; 9 = bare land (data source: HRLULC ver. 16.09 [82]).

2.2. Data

To test S1's capabilities for landslide detection, S1 imagery was downloaded from NASA's Alaska Satellite Facility server [84] as input data. Specifically, 30 images were acquired in ascending (68 relative orbit) and descending mode (46 relative orbit) during the year 2018 (Figure 4). The images were downloaded as Level-1 Single Look Complex (SLC) data.

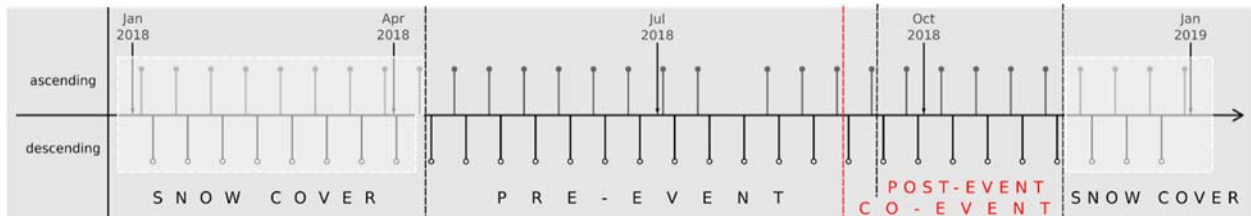


Figure 4. Temporal spacing of S1 acquisitions according to the geometries and the main landslide event (indicated by a red dashed line).

Since snow cover can change both the backscatter of the surface and the sensor–target distance, imagery taken during the snow cover period were removed from the image stacks. The selection of the images to be removed was based on ECMWF ERA-Interim ‘Snow depth’ data downloaded from the ECMWF data dissemination service [85] and S2 imagery of Sentinel Playground [86].

Ascending images before 22 April and after 12 November and descending images before 14 April and after 16 November were rejected because of the presence of snow. Although the remaining images were processed as stacks according to geometries (see next section), both image stacks were later separated into pre-event, co-event, and post-event imageries. The pre-event images (11 ascending and 12 descending) were acquired before the seismic event (as such, not affected by the slides) (Figure 4). The co-event imagery (6 ascending and 7 descending) contains the first image of the event and subsequent S1 images. Post-event imagery (5 ascending and 6 descending) refers to all acquisitions after the event, except the first image after the appearance of the landslides. It should also be mentioned that the complete image stacks for each geometry were analysed separately.

A 5 m resolution DEM provided by the GSI [87] was used for interferometric data processing and later for image classification. In addition, a land use/land cover map of Japan with a resolution of 10 m (HRLULC ver. 16.09 [82,88]) was integrated into the image classification. As ground truth, landslide inventory published by Zhang et al. [76,89] was used.

2.3. Methods

2.3.1. A Priori Considerations

The detection of land cover changes is generally one of the fundamental applications of remote sensing data [90] and is also playing an increasingly important role in the specialised field of SAR remote sensing. When using SAR sensors, the backscattered signal intensity variation in most cases is considered a key indicator of changes. Change detection with SAR images has several advantages. The most important is that the SAR systems are coherent. Due to this technical advantage, the phase differences of the image pixels are estimated from the repeat pass image pairs. For this reason, InSAR coherence is commonly used for change detection [91]. Observing the degree of SAR image pixel similarity, it is possible to estimate the sample complex cross-correlation coefficient between the SAR image pairs:

$$\gamma = \frac{|\sum s_1(x) \cdot s_2(x)^*|}{\sqrt{\sum |s_1(x)|^2 \cdot \sum |s_2(x)|^2}}$$

where γ is the coherence, and s_1 and s_2 two coregistered complex SAR images. The coherence ranges from 0.0 (meaning total decorrelation, phase is random) to 1 (meaning no significant changes, phase correlation is preserved) [92].

In addition to the theoretical considerations, other important assumptions should be taken into account. We assumed that most of the areas were covered with dense forests on the pre-event acquisitions. In this case, the signal backscatter was characterised by continuous small-scale changes due to the variation in the tree canopy surface, resulting in the low coherence of these targets over time (Figure 5). Sudden landslides caused dramatic changes in ground cover and, consequently, in the backscattered signal as well. The change in surface geometry with the removal of forests and topsoil further reduced the coherence. Therefore, the difference between the pre- and post-event coherences should reflect significant changes where landslides occurred. As the landslides developed, smooth surfaces without any vegetation or major irregularities were formed, which could provide stable signal returns and high coherence after the event. The high coherence of post-event imagery compared with pre-event coherences could be a good indicator for landslides. On the other hand, the landslide deposits were often mixed with woody debris, resulting in low coherence.

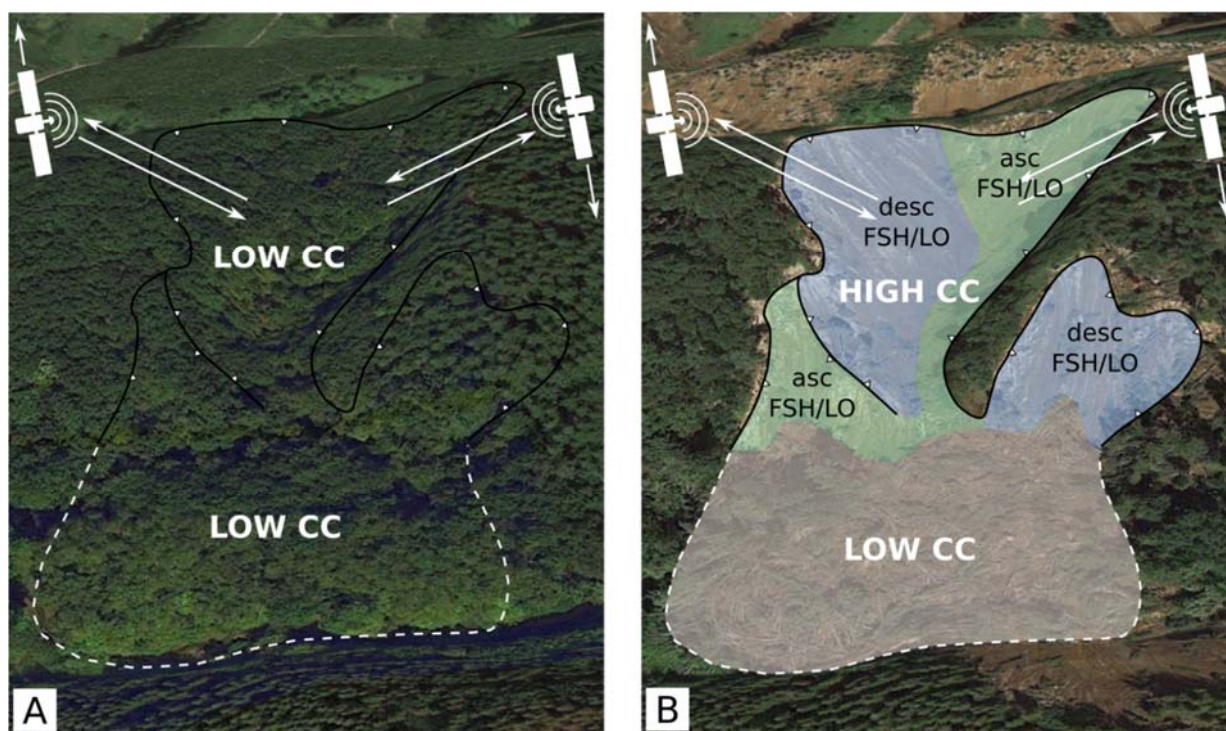


Figure 5. Sketch of coherence changes and the limitations induced by the acquisition geometries triggered by suddenly developed landslide in Hokkaido. (A) = pre-event optical image; (B) = post-event optical image; CC = coherence; asc. = ascending; desc. = descending; FSH/LO = expected foreshortening/layover according to the geometry. The dashed line indicates the mass of the landslide, while the zig-zag line represents the main scarps.

Following these theoretical considerations, we focused our investigation exclusively on the comparison of pre- and co-event and pre- and post-event coherence. In these particular contexts, and considering the roughness of the debris that was covering the slopes after the sliding events, the intensity of the backscatter signal was not affected by significant changes. Therefore, the use of intensity as an indicator of change was excluded.

In addition, multitemporal features (MTF) of coherence pairs were introduced and compared to compensate for the frequent variations in coherence, observed in single coherence pairs.

One of the main drawbacks of the applied technology is the presence of shadows and layover in hilly terrain due to the SAR acquisition geometry, which can corrupt coherence results due to image distortions in case of layover and does not provide information from the field in case of shadows. Shadow and layover occur both before and after the event depending on topography. Therefore, shadow and layover surfaces were masked according to the geometries and ascending and descending shadow/layover-free end results were fused later.

2.3.2. Image Processing

In the first step of the processing, the preselected ascending and descending images were imported into the Envi 5.6. SARscape 5.5.4. and orbit data were applied to the images at the same time (step 2 in Figure 6). The Sentinel-1 input frames were cropped to a defined area of interest corresponding to that of a previous study based on ALOS-PALSAR imagery [73–75]. The 5 m resolution DEM and the mask of the research area were used to crop the images before performing the further steps.

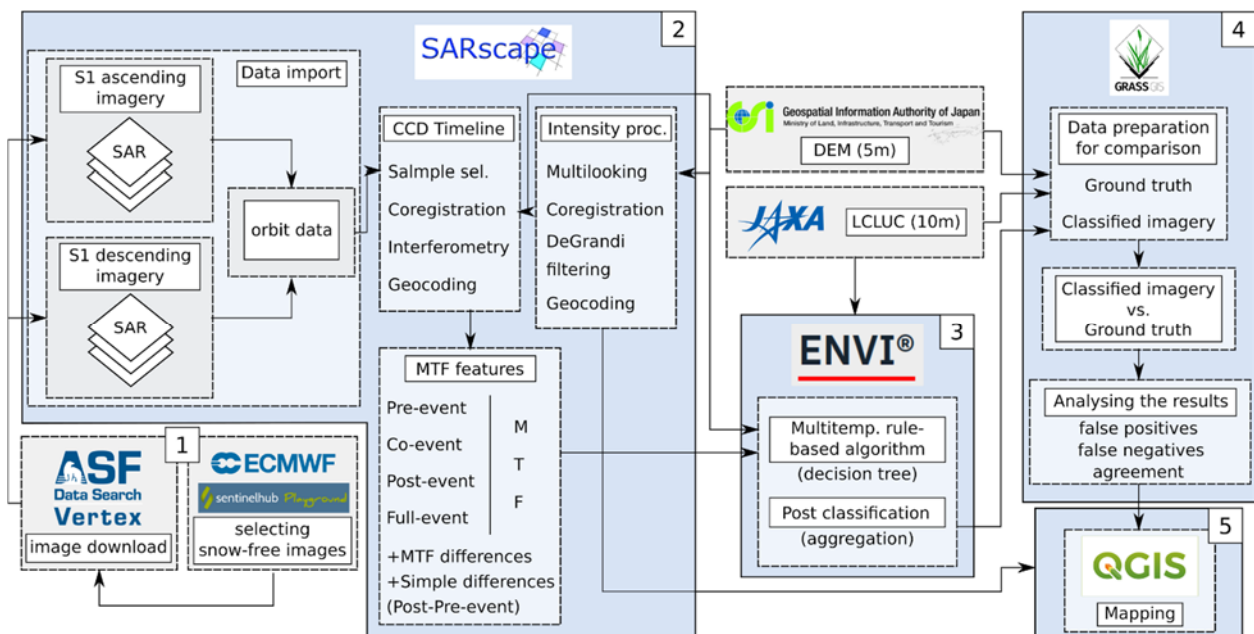


Figure 6. Scheme of data download and processing workflow. 1 = data selection and download, 2 = data import, coherence processing, multi-temporal feature extraction, 3 = image classification, 4 = comparing classified images with ground truth, 5 = map preparation.

The Coherence Change Detection (CCD) TimeLine workflow was run to calculate coherence maps of successive image pairs. The CCD TimeLine processing chain involves an initial data co-registration followed by the interferometric step to produce coherence maps. It should be noted that coherence was calculated through a Boxcar approach in a 5×5 matrix to improve the signal to noise ratio. Shadow and layover maps were also calculated to mask the pixels that were affected by possible distortion of the signal before the following steps were performed. As a last step of the process, the coherence and shadow-layover maps were geocoded with a 15 m spatial resolution.

The Intensity Time Series module of SARscape was used to calculate intensity changes across the site in VV and VH polarisation in both geometries. The sample selected images were first multilooked, coregistered, and filtered with the DeGrandi spatio-temporal filter [93]. Finally, geocoding and radiometric calibration of the images was performed with 15 m spatial resolution.

One of the cornerstones of change detection is time series analysis. It can identify different processes in the land cover transition. Multi-temporal features (MTF) are specific temporal descriptors of different land cover change processes. Well-chosen features can

describe different trends on the surface [94]. The MTF were calculated on pre-, co-, post-, and full-event coherences. The applied MTF were thresholded using the distribution of the pixel value of successfully identified pixels to improve the quality of the classification. Technically, this was a semi-mechanical approach where the MTF thresholding results were continuously compared to the reference data provided by GSI to fine-tune the final thresholds. Three threshold values of MTF were summarized within a decision tree during the subsequent classification. Therefore, thresholds of three MTF images (co-, post- and pre-event) were defined at both geometries (Table 1).

Table 1. Thresholds for multi-temporal coherence features and pre-and post-event coherence differences used during the classification according to event types and geometries.

	Event-Type	Calculated Feature	Ascending Threshold	Descending Threshold
MTF	Co-event	mean	>0.3	>0.3
		maximum	>0.45	>0.45
		span difference	>0.4	>0.4
	Post-event	minimum	>0.175	>0.175
		mean	>0.3	>0.35
		maximum	>0.45	>0.5
	Full event	maximum	>0.45	>0.55
		mean	>0.21	>0.25
		standard deviation	>0.12	>0.125
MTF differences	Co-event Pre-event difference	mean	>0.1	>0.1
		maximum	>0.15	>0.175
		standard deviation	>0.075	>0.075
	Post-event Pre-event difference	minimum	>0.1	>0.1
		mean	>0.14	>0.125
		maximum	>0.14	>0.15
Post-Pre event coherence difference			>0.2	>0.2

To improve landslide detection, co-pre- and post-pre-event coherences were also compared using the following method: First, multi-temporal descriptors of the coherence of the pre-, co-, and post-events were generated. Then, differences of the coherence descriptors of pre-event and co-event, and pre-event and post-event were calculated separately. In the next step, thresholds were applied to the differences of the coherence descriptors (Table 1). Therefore, three thresholded descriptors defined the co-event-pre-event MTF difference image and the other three thresholded descriptors defined the post-event-pre-event MTF difference image. These descriptors were summarized in both cases within a decision tree.

Single pre-co- and pre-post-event coherence images (generated from image pairs) were also calculated. However, due to the very low coherence values, pre-co-event coherence differences were not considered for further analysis. Therefore, their threshold values were excluded from the table, and only post-pre-event coherence differences were retained for further consideration. All of the above coherence differences were calculated using the Band Math tool of Envi.

2.3.3. Image Classification and Post-Processing

Shadow and layover pixels, which were detected during the coherence processing, were removed from the imagery as the first step of the image classification. The masking

procedure was continued with the removal of all LULC pixels except for the three forest categories. This procedure was necessary due to the strong influence of agricultural fields on the results, as frequent coherence changes occurred at rice paddies, grasslands, and crops. Therefore, these fields could not be separated from landslides based on coherence alone. The final step of data preparation (Figure 7) is to remove the portion of the slope with an elevation below 75 m a.s.l. and adding a 7° incline to exclude flat areas that are not prone to landslides.

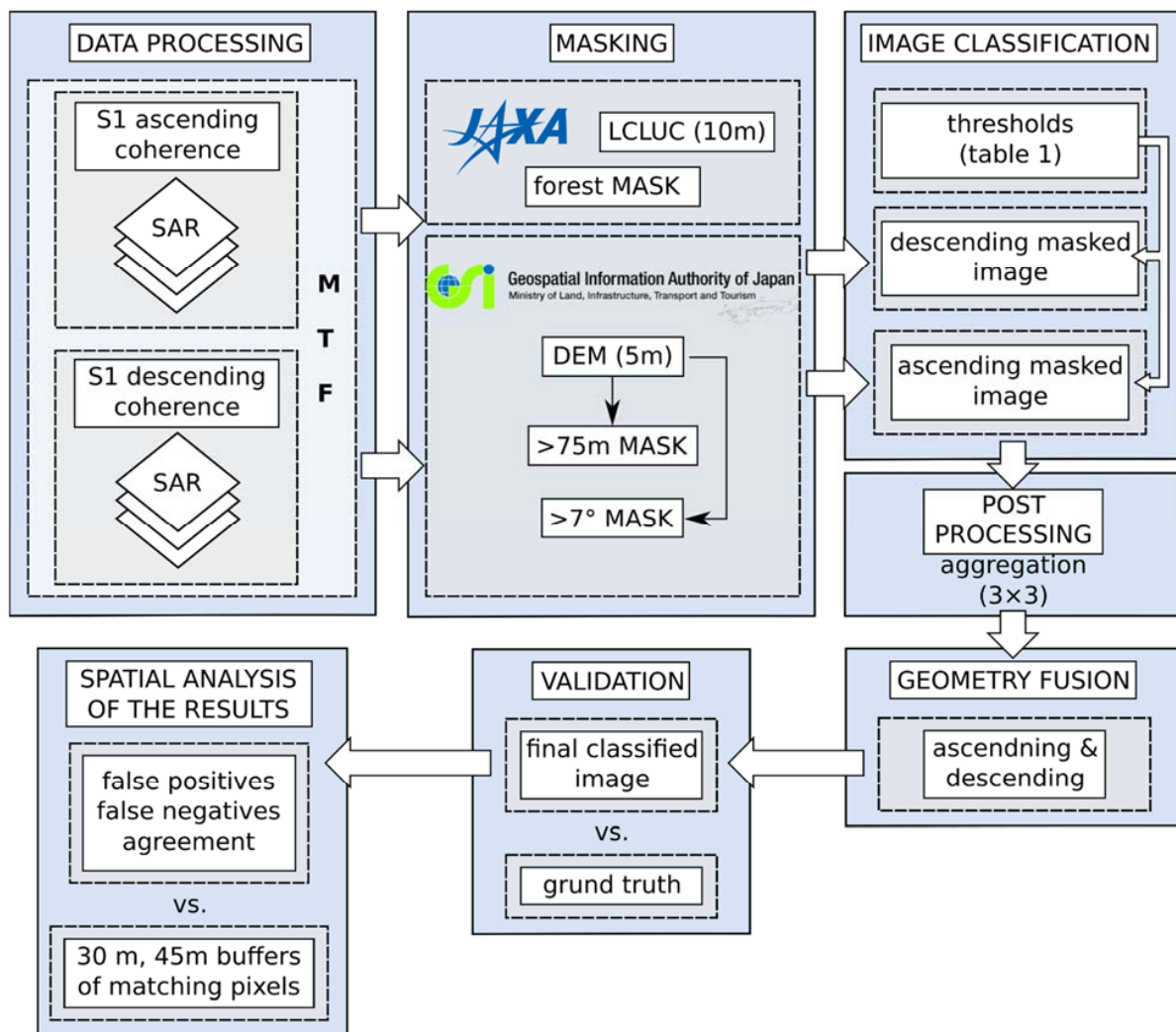


Figure 7. Scheme of image classification and following processing steps.

After masking the images, decision three-based classification was performed according to the thresholds defined in Table 1. The aggregation of individual pixels (Post Classification, Aggregation) followed the classification using a 3×3 matrix to reduce the presence of sparse pixels.

In the fourth step of the workflow (box 4 in Figure 6), the classified images were compared to the ground truth data using simple Boolean algebra provided by Grass GIS. A comparison was performed separately according to geometries, and geometries were fused later and compared to ground truth. The validation was performed at a resolution of 15 m to meet the lower resolution S1 (15 m) with the high-resolution control data [76]. Ground truth areas were used to identify false negatives (pixels that are landslides but were not detected), false positives (pixels that were falsely detected as landslides), and accurately classified pixels (agreement). The areas of valid pixels and false negatives were separately compared to the landslide ground truth, while the proportions of false positives were compared to the

area of the research site (excluding landslides) [95]. Due to the significant portions of false positives, the false negatives and their relation to the well-identified pixels were examined. Therefore, the proportion of false negatives and positives within the 30 and 45 m zones of the agreement were calculated. In addition, the proportions of pre-event topographic elements were also determined in case of false positives, false negatives and the agreements. To calculate topographic elements, the *r.geomorphon* module [83] of GRASS GIS 7.8.2 was used based on the 5 m resolution DEM. Final results were visualised using QGIS 3.10.

3. Results

3.1. Temporal Changes in Intensity

Continuous changes in intensity values were observed over the whole site in both polarisations and geometries (Figure 8). Most of the selected sampling points of LULC categories reflected similar temporal intensity patterns. However, the intensity values of the VV polarisation are one order of magnitude higher than those of the VH polarisation. Furthermore, it is clearly visible in the graphs that these LULC categories cannot be separated from each other considering the intensity of the site due to the overlap of the intensity curves. Therefore, intensity images were not included in further analysis.

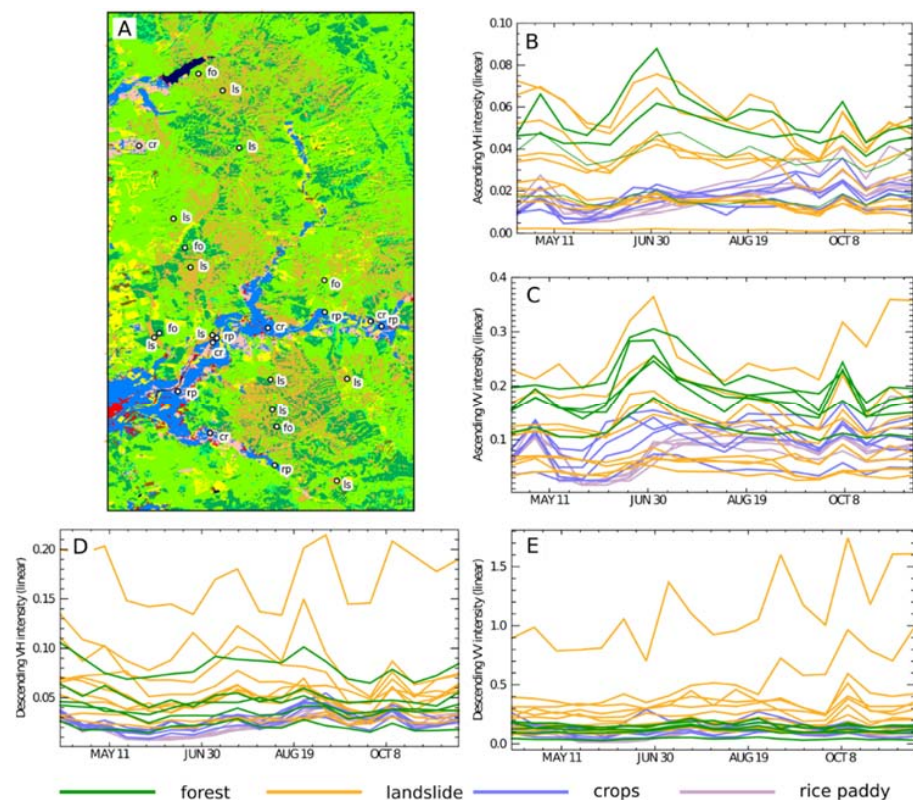


Figure 8. Temporal changes in the intensity of landslide (ls, orange), forest (fo, green), crop field (cr, pink) and rice paddy (rp, blue) samples. (Top left map contains the location of the samples.) (A) = LULC map of the site (see Figures 1 and 3 for legend); (B–E) = intensity time series: (B) = VH, ascending geometry; (C) = VV, ascending geometry; (D) = VH, descending geometry; (E) = VV, descending geometry. Please note, that the y axis of the plots is different for each geometry and polarisation.

3.2. Temporal Changes of the Coherence over the Study Site

As shown in Figure 9, the development of landslides led to a drastic change in the coherence of the affected surfaces. In general, coherence suddenly dropped after the event (visible in co-event images) and later increased on post-event coherence pairs in both geometries. These changes are well identifiable on the graphs of the same figure

(‘asc_landslide’ and ‘desc_landslide’ curves). However, similar changes in coherence were parallely observed on surfaces that were not affected by the event. In fact, agricultural fields (crops, rice paddies and grasslands) show similar temporal behaviour of the coherence at the same time. This means that the landslides and other landscape features behaving similarly could not be separated even when using multitemporal descriptors of the coherence time series. This fact fundamentally controls the potential identification strategies for landslide-affected areas. More than 90% of the landslide area was primarily forested where the pre-event coherences were usually below 0.3 with small fluctuations. Post-event coherences reached ca. 0.5 and higher values here with moderate fluctuations. Therefore, a clear temporal difference of pre- and post-event coherences was identified in the case of forest cover, which unfortunately does not apply to landslides affecting other land use categories. Hence, we focused exclusively on the identification of landslides over forested areas, thus retaining more than 90% of the landslides.

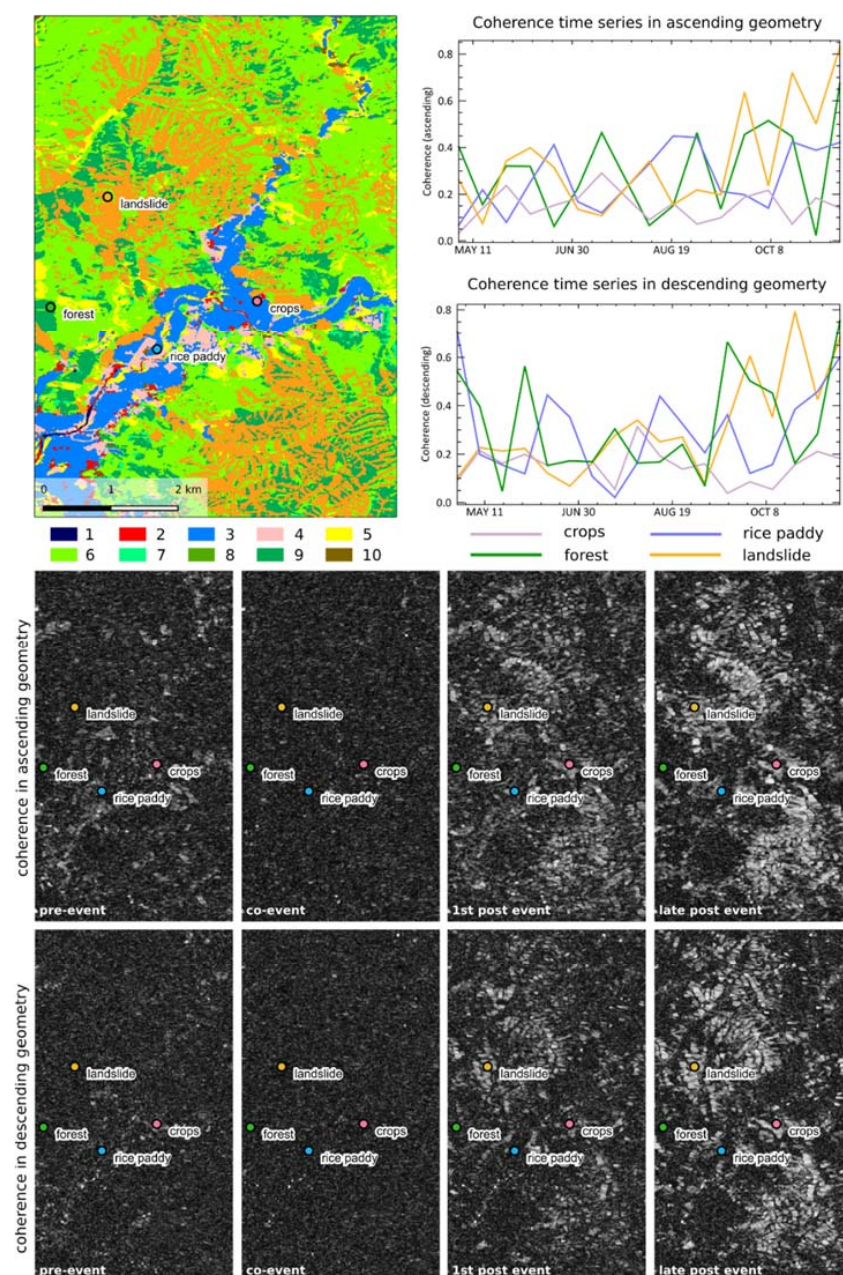


Figure 9. Temporal change of the coherence in ascending and descending geometries. Legend: 1 = water; 2 = urban and built-up; 3 = rice paddy; 4 = crops; 5 = grassland; 6 = deciduous broadleaf

forest; 7 = deciduous needle-leaf forest; 8 = evergreen broadleaf forest; 9 = evergreen needle-leaf forest; 10 = bare land (data source: HRLULC ver. 16.09 [82]). The upper left figure shows the LULC of the site and sampling points (see Figures 1 and 3 for legend). Upper right graphs represent the time series of the coherence at the selected points in 2018 in ascending and descending geometry (full coherence image stack was sampled). The two lower image series present the coherence of the site at four selected time periods (single samples from events) in ascending and descending imagery. (Coherence pairs before classification.) ls = landslide; fo = forest; rp = rice paddy; cr = crops.

3.3. Image Classification Results

Pre- and co-event image differences were discarded because of the low values of the coherence images in both geometries. Therefore, pre- and post-event coherence differences were calculated and classified (Tables 2 and 3). Despite the rejection of the lowest quality pre-co-event coherence pairs, the remaining pre- and post-event image differences provided the lowest quality results, with a weak agreement with the control data (35–42%) and high proportions of false positives (6–9%).

Table 2. Results of classification on ascending geometry data. (The best match is marked in bold text).

Geometry	Feature Type	Event Type	False Negative %	False Positive %	Match %
Ascending	MTF	co	47.843	5.7192	52.1569
		post	51.2658	6.5564	48.7341
		full	38.4679	9.4082	61.5319
	MTF differences	Co-Pre	55.5643	4.0258	44.4356
		Post-Pre	52.4908	5.028	47.5091
	Post-Pre event coherence difference	Post-Pre	57.7057	9.2115	42.2942

Table 3. Results of classification on descending geometry data. (The best match is marked in bold text).

Geometry	Feature Type	Event Type	False Negative %	False Positive %	Match %
Descending	MTF	co	42.2337	6.389	56.5002
		post	51.9506	4.9792	46.7833
		full	47.7736	6.2605	50.9602
	MTF differences	Co-Pre	57.4704	4.1647	41.2635
		Post-Pre	51.69	4.8705	47.0495
	Post-Pre event coherence difference	Post-Pre	63.6516	6.7891	35.0823

The use of MTF in both geometries provided the best classification results. Classified MTF reached 48–61% of correctly classified landslides, while the proportion of false negatives remained at 38–50%, while the proportion of false positives varied between 5–9% in ascending geometry. In descending geometry, the proportion of agreement ranged from 46 to 56%, false negatives reached 42–51%, while the proportion of false positives was about 4–6%. The classification of MTF differences provided lower quality results considering first the proportion of agreement (41–47%), while the proportion of unidentified pixels (false negatives) was higher (52–57%). On the other hand, we found the lowest proportion of false positives here (4–5%).

The highest quality result was obtained by classifying the MTF of the full image stack in ascending geometry. Here, the proportion of the agreement is the highest at 61%, the false negatives occur in only 38%, but the proportion of false positives is also high (9%). In descending geometry, the classification of the MTF of co-event imagery provided the highest quality results (Figure 10). The proportion of agreement reached 56% here, the proportion of false negatives was 42% and false positives were detected in 6%.

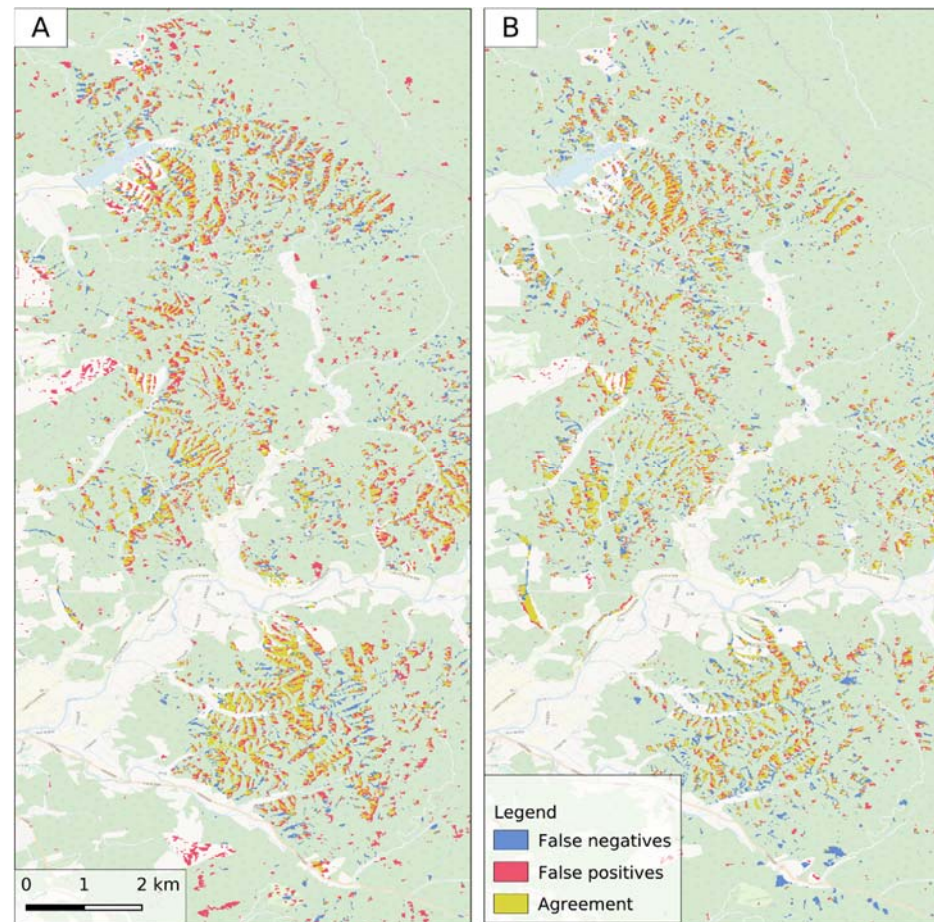


Figure 10. Results of image classification in ascending (A) and descending (B) geometries. (A), the classification of the MTF of the full event. (B), the classification of MTF of the co-event imagery. © OpenStreetMap contributors.

The above-mentioned trends in the classification results remained almost constant, while the ascending and descending classifications were fused. Simple coherence differences provided the lowest quality classification. In the case of MTF differences, the proportion of agreement reached only 43–48%, the proportion of false negatives fluctuated between 56 and 51%, and the proportion of the false positives again remained the lowest (4–5%) of all the fused images. MTF provided better results in the case of landslide recognition (48–57% of agreement, 42–51% of false negatives), while the proportion of false positives was again higher compared to results (6–8%).

The highest result was obtained with the combination of the ascending full-event MTF-based classification and the descending co-event MTF-based imagery. Here, the proportion of agreement reaches more than 60% (about 40% of false negatives) and the proportion of false positives remains at 8.5%.

The significant number of false negatives and false positives should be further investigated. Since the coherence was calculated in a spatial convolution matrix, we can assume that instead of a single-pixel calculation, we have to introduce a buffer zone around the correctly classified pixel. According to the calculations, 58.5% of the false positives

lie in the 30 m buffer zone of the agreement (Figure 11). Furthermore, 67.2% of the false positives lie in the 45 m buffer zone of the agreement. Other false positive pixels appear sporadically outside of the buffer zone and are spatially distributed across the study area. Only the southern part of the area shows higher concentrations of false-positive pixels. False negatives show similar spatial behaviour where 46.9% of them are located in the 30 m buffer zone of the agreement and 56.5% of them lie in the 45 m buffer zone. They are as sporadic as the false positive pixels are outside the buffer zones and false negatives have the same concentration in the southern part of the site.

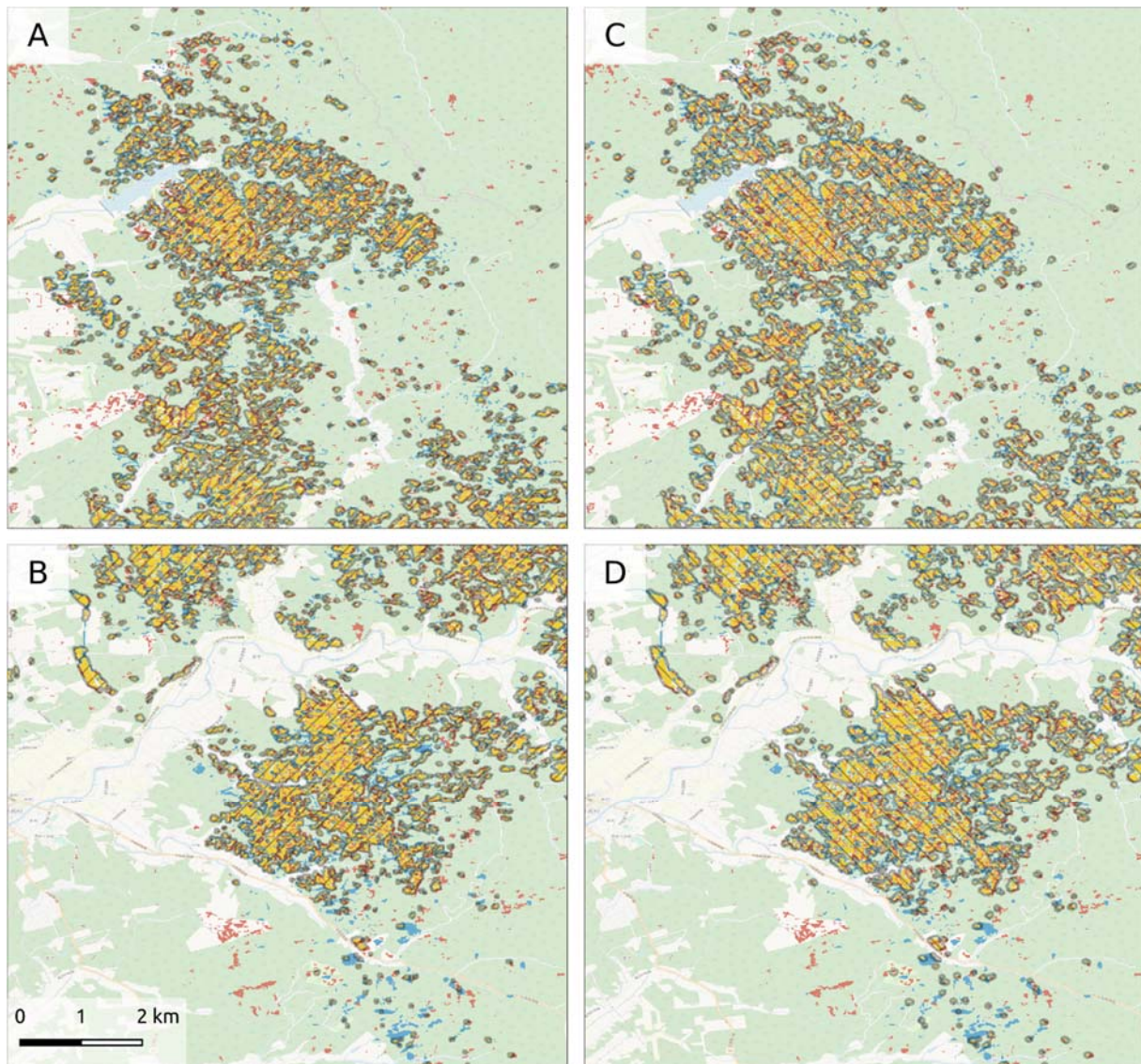


Figure 11. False negatives, false positives, and agreement of the classification results with the 30 m (A,B) and 45 m (C,D) buffer zone of the agreement. © OpenStreetMap contributors.

Figure 12 shows which type of classification result was situated in which terrain form category. A total of 31% of the agreement lies on slopes, 21% on valleys, 16–17% of them on spurs and hollows and 9% on ridges. False negatives were identified on surfaces composed of approximately 30% of valleys, 27% of slopes, 13–16% of spurs, and hollows, and 6% of ridges. A total of 36% of false positives area developed on ridges, 23% on spurs, 24% on slopes and only 6–9% in valleys and hollows.

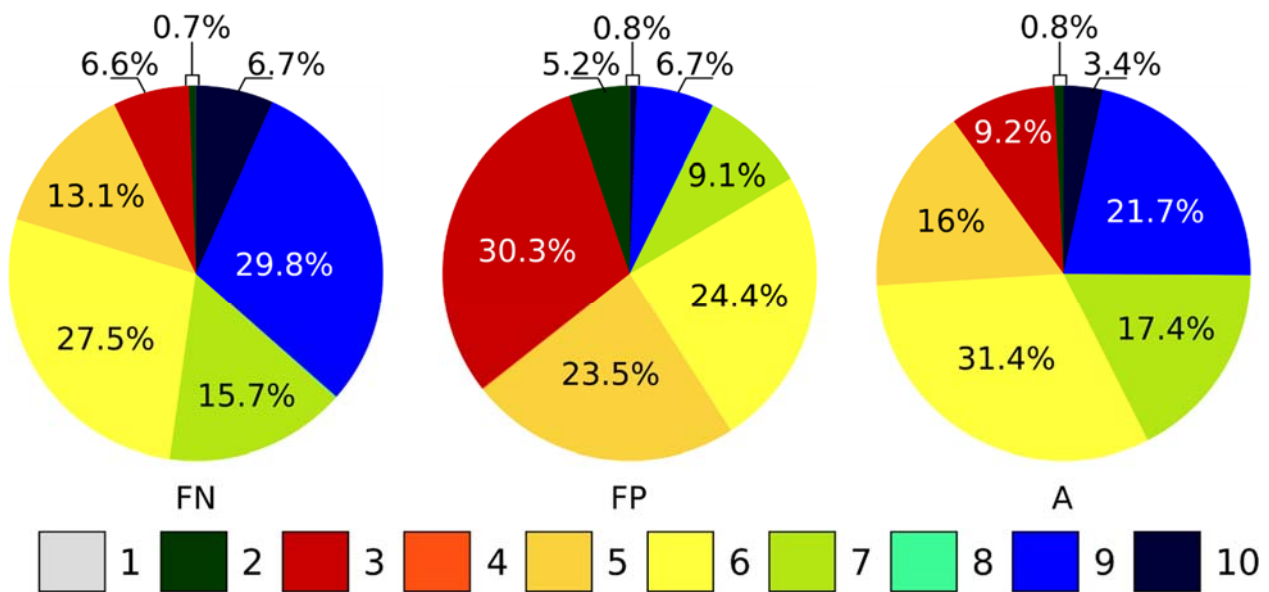


Figure 12. The distribution of terrain forms over false negatives (FN), false positives (FP) and agreement (A) of the most successful classification. 1 = flat; 2 = summit; 3 = ridge; 4 = shoulder; 5 = spur; 6 = slope; 7 = hollow; 8 = footslope; 9 = valley; 10 = depression. Terrain forms were calculated and named after Jasiewicz and Stepinski [83].

4. Discussion

This section focuses on the discussion of the results with special attention to the nature of coherence processing and classification. Furthermore, the results of intensity processing, the role of adequate input data for the processing steps (e.g., SAR images, LULC, etc.), terrain form analysis, and S1 capabilities are discussed. The chapter is structured to systematically answer the questions posed at the end of the introduction.

Question 1. Is it possible to use S1 imagery to detect sudden landslides?

Answer 1. The results indicate that the application of the S1 sensor cannot provide a perfect solution for the detection of sudden landslides at the given site due to the involvement of more than one post-event image and the limitations of the sensor. However, it can approximate the size of landslide-affected areas with considerable overestimation.

Co-event coherence images provide poor results (30–40% of agreement and a high proportion of false positives). Therefore, a rapid response and landslide detection are not possible based on S1 coherence imagery, and even using the first post-event image does not increase the quality of landslide detection at a given location. Coherence degradation would be more visible in areas with better pre-event coherence, and therefore the technique would be applicable in, for example, a built-up environment. Therefore, the technique is again less suitable for accurate quick detection purposes at the given location.

Question 2. What types of features/parameters computed from SAR imagery can effectively describe and map landslides?

Answer 2. Coherence images calculated from pre- and post-event images pairs supplied poor results, while the application of MTF significantly improved the results. Nevertheless, researchers still need to carefully select and fine-tune the site-specific features that can be applied to the given site, such as the size of the convolutional matrix of coherence, the applicable MTFs, the coherence thresholds in ascending and descending geometry, and the DEM and LULC base maps.

Using the MTF of coherence image stacks significantly improved the results compared to single coherence image pairs which had been the only option previously. However, this technique required a significant amount of post-event imagery, on which the coherence of the landslides was improved.

The relatively low proportion of marching pixels and the high proportion of false positives could be an indication of the low quality of the classification results. Nonetheless, more than 46% of the false positives are within the 30 m buffer zone of agreement, and more than 56% of them are in the 45 m buffer zone of the agreement. Firstly, this could be explained by the low spatial resolution of S1 compared to the size of the landslides. Secondly, the 5×5 convolution matrix of the coherence algorithm, which averages the spatial differences, could be the reason. A 3×3 convolution matrix could also be appropriate to preserve spatial resolution; however, it could increase noise. It should be noted that other authors such as Aimati et al. [73] have used additional filtering on ALOS-PALSAR coherence images, which reduces both noise and spatial resolution. However, this suggests that the size of the convolution matrix should be carefully considered at the beginning of image processing.

Considering the thresholds applied during the classification process, it is worth noting that the best settings of the identified thresholds of the two geometries differ slightly from one another. Firstly, this could be due to the geometric characteristics of the scatterers (which are determined by the geomorphology of the site). Secondly, this also suggests that it is hardly possible to formulate universal thresholds applicable across different sites for landslide classification.

Having analysed the coherence time series, it became clear that the successful landslide classification requires the exclusion of agricultural fields because rice paddies, crop fields and even grasslands produce similar coherence variations as landslides on co- and pre-event imagery. Unfortunately, the exclusion of croplands resulted in the loss of approximately 9% of the detectable landslides. Even if 9% of the landslide area was significant, it was not possible to distinguish cropland from landslide areas directly using SAR data. It should be mentioned that the LULC map of Japan provided a reliable, high-resolution basis for the masking procedure. However, such LULC maps had been sparsely available in other countries until recently, which could encumber former S1-based landslide identification elsewhere. On the other hand, Sentinel-based world coverage with a 10 m resolution is freely available [96].

The best available 5 m resolution DEM of GSI was used to remove image distortions. On the other hand, despite the high-quality DEM, landslide formation radically altered the surface and led to the significant repositioning of the layover pixels. These newly emerging pixels were not filtered due to the lack of an up-to-date DEM. Even if no current DEM is available due to the nature of the event, users should carefully select the best available DEM that can improve the quality of image processing.

Question 3. What are the limitations, advantages and disadvantages of S1 imagery in the case of coherent change detection for landslide mapping?

Answer 3. The limitations of using S1 for coherent change detection are due to the spatial resolution, temporal separation of the images, the wavelength of S1 and the particular field conditions (size, shape and spatial distribution of the landslides). Therefore, the ca. 15 m resolution is less suitable for the detection of elongated, narrow landslides, such as the ~ 5.6 cm wavelength, which is too sensitive for the successful detection of the features (which here mainly concerns the intensity). On the contrary, the temporal separation and the fact that the images are freely available make the sensor an obvious choice for at least preliminary site investigations. Additionally, as we have seen, it can approximate the landslide-affected areas and perhaps provide even better results when dealing with landslides of greater magnitude elsewhere.

The dramatic coherence change triggered by the event occurred not only at landslides but was visible all over the study area. Furthermore, large-scale changes occurred time after time in post-event coherence images over the landslides. On one hand, the decrease in overall coherence eliminated the possibility to identify the landslide areas using only the pre- and post-event coherence differences, or only the coherence based on pre- and post-event coherence pairs. On the other hand, the coherence stability of post-event imagery was also questionable and affected the applicability of multi-temporal features. The first

problem could be caused by the dense vegetation cover, which provided low (less than 0.3 on average) coherence. Fujiwara et al. [74] observed the same phenomenon on ALOS-PALSAR coherence imagery. Thus, the changes occurred in this low coherence area, where the phase was less stable, making it very difficult to measure them. The fluctuations in coherence could be due to the displacement of unconsolidated landslide material on the slip surface [74] or the erosion of the slip surface. Thirdly, we should consider that the water content of the topsoil changed temporarily after the event, which determined the penetration depth of the bare slip surfaces. Moreover, the spatial variability of soil water content is probably due to the physical heterogeneity of the suddenly developed landforms (bedrock, altitudinal position, aspect, etc.). Therefore, soil water content could influence the coherence of the landslides. It should also be considered that the landslides triggered not only the downward movement of the topsoil layers. Vegetation is usually transported to the valley floors, mixed with or covering the landslide material. These wrung tree trunks and other tree remnants reflected similar signals towards the sensor as intact forests on the pre-event images.

At first glance, the poorer results obtained with S1 image stacks contradict the findings of Aimati et al. [73], Fujiwara et al. [74], Jung and Yun [75], who used ALOS-PALSAR imagery for the same purpose, and found that intensity is the indicator that gives the best results in landslide detection. The main reason for the unsuccessful intensity analysis could be the short wavelength of the S1 compared to ALOS-PALSAR data. The sensor offers a lower penetration rate, and the short wavelength is more sensitive to small-scale changes. In addition, the changing moisture content of the topsoil layers (or bare bedrock layers of slip surfaces) could strongly influence the surface dielectric constant. Therefore, backscatter intensity could reflect the soil moisture pattern rather than the actual LULC changes.

Regarding the classification results and topographic elements, it is clear that 28% of the landslides affected valleys, but only 21% of the agreements and more than 29% of the false positives were located in valleys in pre-event times. First, narrow valley bottoms hindered landslide detection, as the spatial resolution of S1 is only 15 m. Second, as mentioned above, landslide debris moved along valley floors and was mixed with tree trunks, the complex geometry of which made it very difficult to separate the landslide deposits from surrounding intact forests. Similar trends were observed on slopes, spurs and ridges, which played a significant role in the detection of pre-event surface elements, where landslides developed. However, their role was more pronounced in the false positives. They could be considered as different types (convex, concave), but still as slope elements of the surface, where most false positives occurred during the calculations. Slopes can cause serious image distortions due to the side-looking geometry of the SAR imagery, which were compensated here, by removing shadow and layover pixels in the very first step of image classification. Therefore, spatial resolution, accuracy and timeliness of the DEM applied during the processing have an important impact on the quality of the final result.

Question 4. Do we need higher spatial resolution imagery (such as ALOS-PALSAR) or can S1-based change detection techniques produce adequate results?

Answer 4. Since higher resolution sensors provided better results than S1 during landslide detection, the answer is undoubtedly yes. A sensor with better spatial resolution can provide more details from the surface and the detection can be more accurate. However, we should also consider the wavelength (thus the sensitivity) of the sensor as well as the temporal separation of the images. S1 performance is better taking into account the temporal separation of the images, as well as the freely available images, providing excellent raw material for long-term coherence and intensity investigations. However, the ALOS-Palsar sensor was an adequate choice of previous authors due to its better spatial resolution and longer wavelength. In an ideal case, a more advanced system will involve satellites, which simultaneously and frequently cover the same area on different wavelengths (C and L), with higher spatial resolution (3–5 m) in two geometries.

Considering former papers on the landslide detection of the site, the S1 coherence-based classification results seem to be ambiguous. Firstly, Fujiwara et al. [74] and Aimati

et al. [73] used co-event pre-event coherence differences and normalised where the success rate was analogous to the presented approach (cf. Table 2 in [73]). However, Aimati et al. [73] and Jung and Yun [75] significantly improved their results by evaluating the intensity and multitemporal features of the coherence. In the case of the ALOS-PALSAR imagery, the main advantage of the sensor is its high spatial resolution, which in some cases should be strongly filtered [73]. The main disadvantage of the same sensor is the low temporal resolution, which triggers temporal decorrelation and encumbers multi-temporal coherence analysis. On the one hand, all the authors indicated that intensity processing or multi-temporal analysis of the intensity could be the solution for detecting landslides of the site. On the other hand, S1 is more sensitive to small-scale changes with a lower resolution. Therefore, S1-based intensity processing will not provide better quality results than coherence analysis of the same imagery.

The temporal separation of S1 images can also vary with region. While S1 images are acquired every 6 days all over Europe in both geometries, the temporal lag between images is 12 days over Japan, and this temporal decorrelation significantly affects the quality of change detection. On the other hand, the temporal separation of S1 is better than that of other SAR missions, such as ALOS-PALSAR, where the temporal decorrelation was evidenced [73] at the same site.

According to the review of the literature and our experiences related to this specific topic, we summarize the most relevant aspects of Sentinel-1 and ALOS-PALSAR satellites (Table 4) regarding landslide detection purposes. This comparison is based on a relative scale (1–5/poor–excellent). We are aware that it contains a certain level of subjectivity, but a general overview could support the efforts of experts in nearly real-time landslide mapping.

Table 4. Comparison of S1 and ALOS-PALSAR satellites regarding landslide detection purposes [97,98]. Asterisk: relative scale (1–5/poor–excellent).

Features	S1	ALOS-PALSAR
wavelength	***	*****
pixel spacing	***	*****
revisit-coverage frequency	*****	***
data availability (costs)	*****	**
processing time	*****	***
coherence	***	****
intensity	*	*****

5. Conclusions

Considering the results and their discussion, it is obvious that S1 images can be used for landslide detection at the observed site only with strong limitations. Pre- and co-event and pre- and post-event coherence differences provide poor results, with a low number of agreements and a high proportion of false detections. On the other hand, the results were significantly improved by applying the MTF of coherence and almost reached the success rate of the coherence analysis conducted by previous authors using ALOS-PALSAR imagery. Nevertheless, the improvement of MTF coherence results using S1 intensity was not possible, as was performed in the case of ALOS-PALSAR data, due to the general sensitivity of the short wavelength. Similar to the wavelength, the revisit time of S1 is also a factor that strongly affects the coherence reconstruction of the site and the response time of the system considering the quick detection purpose. Compared to Europe, where the temporal separation of images in both geometry is 6 days (between 2016 and 2021), the revisit time over Japan is 12 days, which could improve significantly in the future considering that the country is prone to natural disasters.

It should also be mentioned that apart from the low number of agreements, approximately half of the false positives were detected in the 30–45 m buffer zone of the agreement.

This shows that the spatial resolution of the sensor is not appropriate for an accurate identification. Only a rough approximation of the area affected by the landslides is possible. While the co-event and full-event MTF coherences provided the best approximation of the landslides, it is evident that the sensor and the above-mentioned techniques cannot be used for rapid detection at the given location.

These observations are applicable to the present site and are strongly influenced by the geomorphological (and geometrical) characteristics of the landslides. This means that further testing of S1 could still be relevant for larger-scale landslides. Improving the results is potentially possible by applying the non-adaptive coherence filtering technique, which could significantly raise coherence values. Although the technique is time consuming and computation intensive, there is the potential to obtain more accurate results, with well reconstructed coherence representing surface forms with less noise. In addition, it is worth considering the ESA WorldCover map for image masking, which could significantly improve the results. Moreover, the capabilities of other sensors with higher spatial resolution and different wavelengths, such as SAOCOM, Capella, and ICEYE, should also be explored. The usability of the ROSE-L and Sentinel-1 Next Generation satellites announced by ESA as well as the NISAR announced by NASA for rapid change detection purposes should also be clarified in the future. The intensive development of new SAR sensors will boost the improvement of landslide monitoring and mapping by microwave satellites. For this reason, our article has attempted to establish new ground by investigating the applicability of S1 to facilitate future multi-sensor-based landslide detections.

Author Contributions: Conceptualization, P.P., G.T., P.R. and I.P.K.; Methodology, P.P., G.T., P.R. and I.P.K.; Software, P.P., G.T., P.R. and I.P.K.; Validation, I.P.K., G.T., F.O. and L.R.; Formal Analysis, I.P.K.; Investigation, I.P.K., G.T.; Resources, F.O., G.T., I.P.K. and F.O.; Data Curation, I.P.K.; Writing—Original Draft Preparation, I.P.K., L.R.; Writing—Review and Editing, I.P.K., L.R., G.T., D.M.K., D.L. and P.P.; Visualization, D.M.K., I.P.K.; Supervision, P.P.; Project Administration, D.M.K., I.P.K., D.L.; Funding Acquisition, F.O.; Corresponding Author, D.M.K. All authors have read and agreed to the published version of the manuscript.

Funding: The project has been supported by the European Union, co-financed by the European Social Fund, within EFOP-3.6.1.-16-2016-00004-Comprehensive Development for Implementing Smart Specialization Strategies at the University of Pécs.

Institutional Review Board Statement: Not applicable.

Data Availability Statement: The data will be made available on request.

Acknowledgments: The first author is grateful to sarmap SA for providing ENVI and SARscape licence for the image processing and to sarmap SA colleagues for providing strong scientific support and advice during the research. The authors are grateful to the Geographical Survey Institute of Japan for providing ground truth data of the event. We also thank the reviewers for their work, their thoughtful comments and their efforts to improve the quality of this article.

Conflicts of Interest: The authors declare no conflict of interest.

List of Abbreviations

APS	Atmospheric Phase Screen
CCD	Coherence Change Detection
DEM	Digital Elevation Model
DInSAR	Differential Synthetic Aperture Radar Interferometry
ECMWF	European Centre for Medium-Range Weather Forecasts
ESA	European Space Agency
FSH	Foreshortening
GB-InSAR	Ground-based synthetic aperture radar interferometry
GIS	Geographic Information System

GPS	Global Positioning System
GSJ	Geospatial Information Authority of Japan
InSAR	Synthetic Aperture Radar Interferometry
LIDAR	Light Detection and Ranging
LO	Layover
LULC	Land Use and Land Cover
MTF	Multitemporal features
NASA	National Aeronautics and Space Administration
PS	Permanent Scatterers
PSI	Persistent Scatterers
SAR	Synthetic Aperture Radar
SBAS	Small-Baseline Subsets
SLC	Single Look Complex
TLS	Terrestrial laser scanning

References

- Kirschbaum, D.B.; Adler, R.F.; Hong, Y.; Lerner-Lam, A. Evaluation of a preliminary satellite-based landslide hazard algorithm using global landslide inventories. *Nat. Hazards Earth Syst. Sci.* **2009**, *9*, 673–686. [\[CrossRef\]](#)
- Kirschbaum, D.; Adler, R.; Hong, Y.; Kumar, S.; Peters-Lidard, C.; Lerner-Lam, A. Advances in landslide nowcasting: Evaluation of a global and regional modeling approach. *Environ. Earth Sci.* **2012**, *66*, 1683–1696. [\[CrossRef\]](#)
- Petley, D.; Dunning, S.A.; Rosser, N.J. The analysis of global landslide risk through the creation of a database of worldwide landslide fatalities. In *Landslide Risk Management*; Hungr, O., Fell, R., Couture, R., Eberhardt, E., Eds.; CRC Press: Cambridge, UK, 2005; pp. 367–374. ISBN 9780429151354.
- Petley, D. Global patterns of loss of life from landslides. *Geology* **2012**, *40*, 927–930. [\[CrossRef\]](#)
- Haque, U.; Blum, P.; da Silva, P.F.; Andersen, P.; Pilz, J.; Chalov, S.R.; Malet, J.P.; Auflič, M.J.; Andres, N.; Poyiadji, E.; et al. Fatal landslides in Europe. *Landslides* **2016**, *13*, 1545–1554. [\[CrossRef\]](#)
- Lin, Q.; Wang, Y. Spatial and temporal analysis of a fatal landslide inventory in China from 1950 to 2016. *Landslides* **2018**, *15*, 2357–2372. [\[CrossRef\]](#)
- Gokceoglu, C.; Sezer, E.A. statistical assessment on international landslide literature (1945–2008). *Landslides* **2009**, *6*, 345–351. [\[CrossRef\]](#)
- Guzzetti, F.; Carrara, A.; Cardinali, M.; Reichenbach, P. Landslide hazard evaluation: A review of current techniques and their application in a multi-scale study, Central Italy. *Geomorphology* **1999**, *31*, 181–216. [\[CrossRef\]](#)
- Guzzetti, F.; Reichenbach, P.; Cardinali, M.; Galli, M.; Ardizzone, F. Probabilistic landslide hazard assessment at the basin scale. *Geomorphology* **2005**, *72*, 272–299. [\[CrossRef\]](#)
- Uhlemann, S.; Smith, A.; Chambres, J.; Dixon, N.; Dijkstra, T.; Haslan, E.; Meldrum, P.; Merritt, A.; Gunn, D.; Mackay, J. Assessment of ground-based monitoring techniques applied to landslide investigations. *Geomorphology* **2016**, *253*, 438–451. [\[CrossRef\]](#)
- Van Westen, C.J.; Castellanos, E.; Kuriakose, S.L. Spatial data for landslide susceptibility, hazards and vulnerability assessment: An overview. *Eng. Geol.* **2008**, *102*, 112–131. [\[CrossRef\]](#)
- Carlà, T.; Macciotta, R.; Hendry, M.; Martin, D.; Edwards, T.; Evans, T.; Farina, P.; Intrieri, E.; Casagli, N. Displacement of a landslide retaining wall and application of an enhanced failure forecasting approach. *Landslides* **2018**, *15*, 489–505. [\[CrossRef\]](#)
- Garcia, A.; Hordt, A.; Fabian, M. Landslide monitoring with high resolution tilt measurements at the Dollendorfer Hardt landslide, Germany. *Geomorphology* **2010**, *120*, 16–25. [\[CrossRef\]](#)
- Guerriero, L.; Guadagno, F.M.; Revellino, P. Estimation of earth-slide displacement from GPS-based surface-structure geometry reconstruction. *Landslides* **2018**, *16*, 425–430. [\[CrossRef\]](#)
- Guzzetti, F.; Mondini, A.C.; Cardinali, M.; Fiorucci, F.; Santangelo, M.; Chang, K.T. Landslide inventory maps: New tools for an old problem. *Earth-Sci. Rev.* **2012**, *112*, 42–66. [\[CrossRef\]](#)
- Huang, R.; Jiang, L.; Shen, X.; Dong, Z.; Zhou, Q.; Yang, B.; Wang, H. An efficient method of monitoring slow- moving landslides with long-range terrestrial laser scanning: A case study of the Dashu landslide in the Three Gorges Reservoir Region, China. *Landslides* **2018**, *16*, 839–855. [\[CrossRef\]](#)
- Casagli, N.; Catani, F.; Del Ventisette, C.; Luzi, G. Ground-based Interferometry for landslide monitoring. In *Landslide Dynamics: ISRD-ICL Landslide Interactive Teaching Tools, Volume 1 Fundamentals, Mapping and Monitoring*; Sassa, K., Guzzetti, F., Yamagishi, H., Abranas, Z., Casagli, N., McSaveney, M., Eds.; Springer: Cham, Switzerland, 2015. [\[CrossRef\]](#)
- Savvaïdis, P.D. Existing landslide monitoring systems and techniques. In *From Stars to Earth and Culture, in Honor of the Memory of Professor Alexandros Tsioumis*; The Aristotle University of Thessaloniki: Thessaloniki, Greece, 2003; pp. 242–258.
- Maček, M.; Petkovšek, A.; Bojan, M.; Mikoš, M. Landslide Monitoring Techniques Database. In *World Landslide Forum 3, Beijing, China. Volume: Landslide Science for a Safer Geoenvironment, Vol. 1: The International Programme on Landslides*; Springer: Cham, Switzerland, 2014; pp. 193–197. [\[CrossRef\]](#)
- Angeli, M.G.; Pasuto, A.; Silvano, S. A critical review of landslide monitoring experiences. *Eng. Geol.* **2000**, *55*, 133–147. [\[CrossRef\]](#)

21. Liu, S.; Wang, Z. Choice of surveying methods for landslides monitoring. In *Landslides and Engineered Slopes*; Chen, Z., Zhang, J.-M., Ho, K., Wu, F.-Q., Eds.; Taylor and Francis Group: London, UK, 2008; pp. 1211–1216, ISBN 978-0-415-41196-7.
22. Arbanas, S.M.; Arbanas, Z. Landslide mapping and monitoring: Review of conventional and advanced techniques. In Proceedings of the 4th Symposium of Macedonian Association for Geotechnics, Skopje, North Macedonia, 25–28 June 2014; pp. 57–72.
23. Jaboyedoff, M.; Oppikofer, T.; Abellán, A.; Derron, M.H.; Loye, A.; Metzger, R.; Pedrazzini, A. Use of LIDAR in landslide investigations: A review. *Nat. Hazards* **2012**, *61*, 5–28. [[CrossRef](#)]
24. Zhao, C.; Lu, Z. Remote Sensing of Landslides—A Review. *Remote Sens.* **2018**, *10*, 279. [[CrossRef](#)]
25. Kovács, I.P.; Bugya, T.; Czigány, S.; Defilippi, M.; Dobre, B.; Fábián, S.Á.; Lóczy, D.; Riccardi, P.; Ronczyk, L.; Pasquali, P. Monitoring landslides using C-band interferometry. A case study: Dunaszekcső Landslide, Southern Transdanubia, Hungary. *Studia Geomorphol. Carpatho-Balc.* **2018**, *51–52*, 87–105.
26. Kovács, I.P.; Bugya, T.; Czigány, S.; Defilippi, M.; Lóczy, D.; Riccardi, P.; Ronczyk, L.; Pasquali, P. How to avoid false interpretations of Sentinel-1A TOPSAR interferometric data in landslide mapping? A case study: Recent landslides in Transdanubia, Hungary. *Nat. Hazards* **2018**, *96*, 693–712. [[CrossRef](#)]
27. Glade, T.; Anderson, M.; Crozier, M.J. *Landslide Hazard and Risk*; John Wiley & Sons Ltd.: Chichester, UK, 2005; p. 802.
28. Tofani, V.; Raspini, F.; Catani, F.; Casagli, N. Persistent Scatterer Interferometry (PSI) technique for land-slide characterization and monitoring. *Remote Sens.* **2013**, *5*, 1045–1065. [[CrossRef](#)]
29. Pecoraro, G.; Calvello, M.; Piciullo, L. Monitoring strategies for local landslide early warning systems. *Landslides* **2018**, *16*, 213–231. [[CrossRef](#)]
30. Chae, B.G.; Park, H.J.; Catani, F.; Simoni, A.; Berti, M. Landslide prediction, monitoring and early warning: A concise review of state-of-the-art. *Geosci. J.* **2017**, *21*, 1033–1070. [[CrossRef](#)]
31. Pardeshi, S.D.; Autade, S.E.; Pardeshi, S.S. Landslide hazard assessment: Recent trends and techniques. *SpringerPlus* **2013**, *2*, 523. [[CrossRef](#)]
32. Corominas, J.; van Westen, C.J.; Frattini, P.; Cascini, L.; Malet, J.P.; Fotopoulou, S.; Catani, S.; Van Den Eeckhaut, M.; Mavrouli, O.; Agliardi, F.; et al. Recommendations for the quantitative analysis of landslide risk. *Bull. Eng. Geol. Environ.* **2014**, *73*, 209–263. [[CrossRef](#)]
33. Reichenbach, P.; Rossi, M.; Malamud, B.D.; Mihir, M.; Guzzetti, F. A review of statistically-based landslide susceptibility models. *Earth-Sci. Rev.* **2018**, *180*, 60–91. [[CrossRef](#)]
34. Hein, A. *Processing of SAR Data. Fundamentals, Signal Processing, Interferometry*; Springer: Berlin/Heidelberg, Germany, 2004; p. 291. [[CrossRef](#)]
35. Barra, A.; Monserrat, O.; Mazzanti, P.; Esposito, C.; Crosetto, M.; Mugnozza, G.S. First insights on the potential of Sentinel-1 for landslides detection. *Geomat. Nat. Hazards Risk* **2016**, *7*, 1874–1883. [[CrossRef](#)]
36. Gariano, S.F.; Guzzetti, F. Landslides in a changing climate. *Earth-Sci. Rev.* **2016**, *162*, 227–252. [[CrossRef](#)]
37. Sowter, A.; Bin Che Amat, M.; Cigna, F.; Marsh, S.; Athab, A.; Alshammari, L. Mexico City land subsidence in 2014–2015 with Sentinel-1 IW TOPS: Results using Intermittent SBAS (ISBAS) technique. *Int. J. Appl. Earth Obs. Geoinf.* **2016**, *52*, 230–242. [[CrossRef](#)]
38. Pourghasemi, H.R.; Teimoori Yansari, Z.; Panagos, P.; Pradhan, B. Analysis and evaluation of landslide susceptibility: A review on articles published during 2005–2016 (periods of 2005–2012 and 2013–2016). *Arab. J. Geosci.* **2018**, *11*, 193. [[CrossRef](#)]
39. Lee, S. Current and Future Status of GIS-based Landslide Susceptibility Mapping: A Literature Review. *Korean J. Remote Sens.* **2019**, *35*, 179–193. [[CrossRef](#)]
40. Ferretti, A.; Prati, C.; Rocca, F. Permanent scatterers in SAR interferometry. *Trans. Geosci. Remote Sens.* **2001**, *39*, 8–20. [[CrossRef](#)]
41. Ferretti, A. *Satellite InSAR Data. Reservoir Monitoring from Space*; EAGE Publications: Houten, The Netherlands, 2014; p. 160.
42. Pasquali, P.; Cantone, A.; Riccardi, P.; Defilippi, M.; Ogushi, F.; Gagliano, S.; Tamura, M. Mapping of ground deformations with interferometric stacking techniques. In *Land Applications of Radar Remote Sensing*; Holecz, F., Pasquali, P., Milisavljevic, N., Eds.; InTechOpen: London, UK, 2014; pp. 231–258. [[CrossRef](#)]
43. Piacentini, D.; Devoto, S.; Mantovani, M.; Pasuto, A.; Prampolini, M.; Soldati, M. Landslide susceptibility modeling assisted by Persistent Scatterers Interferometry (PSI): An example from the northwestern coast of Malta. *Nat. Hazards* **2015**, *78*, 681–697. [[CrossRef](#)]
44. Wasowski, J.; Bovenga, F. Remote sensing of landslide motion with emphasis on satellite multitemporal interferometry applications: An overview. In *Landslide Hazards, Risk, and Disasters*; Davies, T., Ed.; Elsevier: Amsterdam, The Netherlands, 2015; pp. 345–403.
45. Wasowski, J.; Bovenga, F. Investigating landslides and unstable slopes with satellite Multi Temporal Interferometry: Current issues and future perspectives. *Eng. Geol.* **2014**, *174*, 103–138. [[CrossRef](#)]
46. Rott, H.; Nagler, T. The contribution of radar interferometry to assessment of landslide hazards. *Adv. Space Res.* **2006**, *37*, 710–719. [[CrossRef](#)]
47. Preiss, M.; Stacy, J.S. *Coherent Change Detection: Theoretical Description and Experimental Results*; Defence Science and Technology Organisation, Intelligence, Surveillance and Reconnaissance Division: Edinburgh, Australia, 2006; p. 104.
48. Dwyer, E.; Monaco, S.; Pasquali, P. An operational forest mapping tool using spaceborne SAR data. In Proceedings of the ERS-ENVISAT Symposium, Gothenburg, Sweden, 16–20 October 2000.

49. Holecz, F.; Barbieri, M.; Cantone, A.; Pasquali, P.; Monaco, S. Synergetic Use of ALOS PALSAR, ENVISAT ASAR and Landsat TM/ETM+ Data for Land Cover and Change Mapping. In *JAXA Kyoto and Carbon Initiative*; Japan Aerospace Exploration Agency, Earth Observation Research Centre: Tokyo, Japan, 2009; p. 6.
50. Kellndorfer, J.; Cartus, O.; Bishop, J.; Walker, W.; Holecz, F. Large scale mapping of forests and land cover with synthetic aperture radar data. In *Land Applications of Radar Remote Sensing*; Closson, D., Holecz, F., Pasquali, P., Milisavljevic, N., Eds.; InTechOpen: London, UK, 2014; pp. 59–94. [[CrossRef](#)]
51. Milisavljević, N.; Collivignarelli, F.; Holecz, F. Estimation of Cultivated Areas Using Multi-Temporal SAR Data. In *Land Applications of Radar Remote Sensing*; Closson, D., Holecz, F., Pasquali, P., Milisavljevic, N., Eds.; InTechOpen: London, UK, 2014; pp. 95–120. [[CrossRef](#)]
52. Milisavljević, N.; Closson, D.; Block, I. Detecting human-induced changes using coherent change detection in SAR images. In *Proceedings of the ISPRS TC VII Symposium, Vienna, Austria, 5–7 July 2010*; Wagner, W., Székely, B., Eds.; Vienna University of Technology: Vienna, Austria, 2010; Volume 38, Part 7B, pp. 387–394.
53. Liu, J.G.; Mason, P.; Hilton, F.; Lee, H. Detection of Rapid Erosion in SE Spain: A GIS Approach Based on ERS SAR Coherence Imagery. *Photogramm. Eng. Remote Sens.* **2004**, *70*, 1179–1185. [[CrossRef](#)]
54. Nico, G.; Pappaleopore, M.; Pasquariello, G.; Refice, A.; Samarelli, S. Comparison of SAR amplitude vs. coherence flood detection methods—a GIS application. *Int. J. Remote Sens.* **2000**, *21*, 1619–1631. [[CrossRef](#)]
55. Atzori, S.; Tolomei, C.; Antonioli, A.; Merryman Boncori, J.P.; Bannister, S.; Trasatti, E.; Pasquali, P.; Salvi, S. The 2010–2011 Canterbury, New Zealand seismic sequence: Multiple source analysis from InSAR data and modeling. *J. Geophys. Res. (Solid Earth)* **2012**, *117*, 1857–1861. [[CrossRef](#)]
56. Washaya, P.; Balz, T. SAR coherence change detection of urban areas affected by disasters using Sentinel-1 imagery. *Int. Arch. Photogramm. Remote Sens. Spat. Inf. Sci.* **2018**, *42*, 1857–1861. [[CrossRef](#)]
57. Washaya, P.; Balz, T.; Mohamadi, B. Coherence Change-Detection with Sentinel-1 for Natural and Anthropogenic Disaster Monitoring in Urban Areas. *Remote Sens.* **2018**, *10*, 1026. [[CrossRef](#)]
58. Tessari, G.; Floris, M.; Pasquali, P. Phase and amplitude analyses of SAR data for landslide detection and monitoring in non-urban areas located in the North-Eastern Italian pre-Alps. *Environ. Earth Sci.* **2017**, *76*, 85. [[CrossRef](#)]
59. Osmanoğlu, B.; Sunar, F.; Wdowinski, S.; Cabral-Cano, E. Time series analysis of InSAR data: Methods and trends. *ISPRS J. Photogramm. Remote Sens.* **2015**, *115*, 90–102. [[CrossRef](#)]
60. Bovenga, F.; Pasquariello, G.; Refice, A. Statistically-Based Trend Analysis of MTInSAR Displacement Time Series. *Remote Sens.* **2021**, *13*, 2302. [[CrossRef](#)]
61. Ghaderpour, E. JUST: MATLAB and python software for change detection and time series analysis. *GPS Solut.* **2021**, *25*, 85. [[CrossRef](#)]
62. Plank, S. Rapid damage assessment by means of multi-temporal SAR—A comprehensive review and outlook to Sentinel-1. *Remote Sens.* **2014**, *6*, 4870–4906. [[CrossRef](#)]
63. Ito, Y.; Hosokawa, M.; Lee, H.; Liu, J.G. Extraction of damaged regions using SAR data and neural networks. *International Archives of Photogrammetry. Remote Sens.* **2000**, *33*, 156–163.
64. Ito, Y.; Hosokawa, M. Damage Estimation Model Using Temporal Coherence Ratio. In *Proceedings of the IEEE IGARSS, Toronto, ON, Canada, 24–28 June 2002*; pp. 2859–2861.
65. Yonezawa, C.; Tomiyama, N.; Takeuchi, S. Urban Damage Detection Using Decorrelation of SAR Interferometric Data. In *Proceedings of the IEEE IGARSS, Toronto, ON, Canada, 24–28 June 2002*; pp. 2051–2053.
66. Hoffmann, J. Mapping damage during the Bam (Iran) earthquake using interferometric coherence. *Int. J. Remote Sens.* **2007**, *28*, 1199–1216. [[CrossRef](#)]
67. Mansouri, B.; Shinozuka, M.; Huyck, C.; Houshmand, B. Earthquake-induced change detection in the 2003 Bam, Iran, earthquake by complex analysis using Envisat ASAR data. *Earthq. Spectra* **2005**, *21*, 275–284. [[CrossRef](#)]
68. Matsuoka, M.; Yamazaki, F. Building damage mapping of the 2003 Bam, Iran, earthquake using Envisat/ASAR intensity imagery. *Earthq. Spectra* **2005**, *21*, 285–294. [[CrossRef](#)]
69. Chini, M.; Bignami, C.; Stramondo, S.; Pierdicca, N. Uplift and subsidence due to the 26 December 2004 Indonesian earthquake detected by SAR data. *Int. J. Remote Sens.* **2008**, *29*, 3891–3910. [[CrossRef](#)]
70. Matsuoka, M.; Yamazaki, F. Application of the Damage Detection Method Using SAR Intensity Images to Recent Earthquakes. In *Proceedings of the IEEE IGARSS, Toronto, ON, Canada, 24–28 June 2002*; pp. 2042–2044.
71. Yonezawa, C.; Takeuchi, S. Decorrelation of SAR data by urban damages caused by the 1995 Hyogoken-nambu earthquake. *Int. J. Remote Sens.* **2001**, *22*, 1585–1600. [[CrossRef](#)]
72. Matsuoka, M.; Yamazaki, F. Characteristics of Satellite SAR Images in the Areas Damaged by Earthquakes. In *Proceedings of the IEEE IGARSS, Honolulu, HI, USA, 24–28 July 2000*; pp. 2693–2696.
73. Aimaiti, Y.; Liu, W.; Yamazaki, F.; Maruyama, Y. Earthquake-induced landslide mapping for the 2018 Hokkaido Eastern Iburu Earthquake using PALSAR-2 data. *Remote Sens.* **2019**, *11*, 2351. [[CrossRef](#)]
74. Fujiwara, S.; Nakano, T.; Morishita, Y.; Kobayashi, T.; Yurai, H.; Une, H.; Hayashi, K. Detection and interpretation of local surface deformation from the 2018 Hokkaido Eastern Iburu Earthquake using ALOS-2 SAR data. *Earth Planets Space* **2019**, *71*, 64. [[CrossRef](#)]

75. Jung, J.; Yun, S. Evaluation of Coherent and Incoherent Landslide Detection Methods Based on Synthetic Aperture Radar for Rapid Response: A Case Study for the 2018 Hokkaido Landslides. *Remote Sens.* **2020**, *12*, 265. [[CrossRef](#)]
76. Zhang, S.; Li, R.; Wang, F.; Iio, A. Characteristics of landslides triggered by the 2018 Hokkaido Eastern Iburi earthquake, Northern Japan. *Landslides* **2019**, *16*, 1691–1708. [[CrossRef](#)]
77. Yamagishi, H.; Yamazaki, F. Landslides by the 2018 Hokkaido Iburi-Tobu Earthquake on September 6. *Landslides* **2018**, *15*, 2521–2524. [[CrossRef](#)]
78. Hirose, W.; Kawakami, G.; Kase, Y.; Ishimaru, S.; Koshimizu, K.; Koyasu, H.; Takahashi, R. Preliminary report of slope movements at Atsuma Town and its surrounding areas caused by the 2018 Hokkaido Eastern Iburi Earthquake. *Rep. Local Indep. Adm. Agency Hokkaido Res. Organ.* **2018**, *90*, 33–44.
79. Wang, F.; Fan, X.; Yunus, A.P.; Subramanian, S.S.; Alonso-Rodriguez, A.; Dai, L.; Xu, Q.; Huang, R. Coseismic landslides triggered by the 2018 Hokkaido, Japan (Mw 6.6), earthquake: Spatial distribution, controlling factors, and possible failure mechanism. *Landslides* **2019**, *16*, 1551–1566. [[CrossRef](#)]
80. Tajika, J.; Ohtsu, S.; Inui, T. Interior structure and sliding process of landslide body composed of stratified pyroclastic fall deposits at the Apporo 1 archaeological site, southeastern margin of the Ishikari Lowland, Hokkaido, North Japan. *J. Geol. Soc. Jpn.* **2016**, *122*, 23–35. [[CrossRef](#)]
81. Kameda, J.; Kamiya, H.; Masumoto, H.; Morisaki, T.; Hiratsuka, T.; Inaoi, C. Fluidized landslides triggered by the liquefaction of subsurface volcanic deposits during the 2018 Iburi-Tobu earthquake, Hokkaido. *Sci. Rep.* **2019**, *9*, 13119. [[CrossRef](#)]
82. Hashimoto, S.; Tadono, T.; Onosato, M.; Hori, M.; Shiomi, K. A New Method to Derive Precise Land-use and Land-cover Maps Using Multi-temporal Optical Data. *J. Remote Sens. Soc. Jpn.* **2014**, *34*, 102–112.
83. Jasiewicz, J.; Stepinski, T. Geomorphons—A pattern recognition approach to classification and mapping of landforms. *Geomorphology* **2013**, *182*, 147–156. [[CrossRef](#)]
84. Alaska Satellite Facility Server. Available online: <https://search.asf.alaska.edu/#/> (accessed on 3 March 2022).
85. European Centre for Medium-Range Weather Forecasts (ECMWF) Data Dissemination Service. Available online: <https://apps.ecmwf.int/datasets/data/interim-full-daily/levtype=sfc/> (accessed on 3 March 2022).
86. Sentinel Playground. Available online: <https://www.sentinel-hub.com/explore/sentinelplayground/> (accessed on 3 March 2022).
87. Geospatial Information Authority of Japan, AW3D Standard. Available online: <https://www.aw3d.jp/en/products/standard/> (accessed on 3 March 2022).
88. ALOS Research and Application Project, High-Resolution Land Use and Land Cover Map Products. Available online: https://www.eorc.jaxa.jp/ALOS/en/dataset/lulc_e.htm (accessed on 3 March 2022).
89. Characteristics of Landslides Triggered by the 2018 Hokkaido Eastern Iburi Earthquake, North Japan. Available online: <https://zenodo.org/record/2577300#.YiInDOjMJhE> (accessed on 3 March 2022).
90. Gutman, G.; Byrnes, R.; Masek, J.; Covington, S.; Justice, C.; Franks, S.; Headley, R. Towards monitoring land cover and land use changes at a global scale: The Global Land Survey 2005. *Photogramm. Eng. Remote Sens.* **2008**, *74*, 6–10.
91. Bouaraba, A.; Milisavljević, N.; Achero, M.; Closson, D. Change Detection and Classification Using High Resolution SAR Interferometry. In *Land Applications of Radar Remote Sensing*; Closson, D., Holecz, F., Pasquali, P., Milisavljevic, N., Eds.; InTechOpen: London, UK, 2014; pp. 149–163. [[CrossRef](#)]
92. Closson, D.; Milisavljevic, N. InSAR Coherence and Intensity Changes Detection. In *Mine Action—The Research Experience of the Royal Military Academy of Belgium*; Beumier, C., Closson, D., Lacroix, V., Milisavljevic, N., Yvinec, Y., Eds.; InTechOpen: London, UK, 2014; pp. 155–176. [[CrossRef](#)]
93. De Grandi, G.F.; Leysen, M.; Lee, J.S.; Schuler, D. Radar reflectivity estimation using multiple SAR scenes of the same target: Technique and applications. In *Proceedings of the IGARSS'97, IEEE International Geoscience and Remote Sensing Symposium Proceedings, Remote Sensing—A Scientific Vision for Sustainable Development, Singapore, 3–8 August 1997; Volume 2*, pp. 1047–1050. [[CrossRef](#)]
94. Campos-Taberner, M.; García-Haro, F.J.; Camps-Valls, G.; Grau-Muedra, G.; Nutini, F.; Busetto, L.; Katsantonis, D.; Stavrakoudis, D.; Minakou, C.; Gatti, L.; et al. Exploitation of SAR and Optical Sentinel Data to Detect Rice Crop and Estimate Seasonal Dynamics of Leaf Area Index. *Remote Sens.* **2017**, *9*, 248. [[CrossRef](#)]
95. Olofsson, P.; Foody, G.M.; Herold, M.; Stehman, S.V.; Woodcock, C.E.; Wulder, M.A. Good practices for estimating area and assessing accuracy of land change. *Remote Sens. Environ.* **2014**, *148*, 42–57. [[CrossRef](#)]
96. ESA WorldCover—Worldwide Land Cover Mapping. Available online: <https://esa-worldcover.org/en> (accessed on 3 March 2022).
97. ALOS Research and Application Project. Available online: https://www.eorc.jaxa.jp/ALOS/en/index_e.htm (accessed on 3 March 2022).
98. The European Space Agency—Sentinel Mission Guide. Available online: <https://sentinel.esa.int/web/sentinel/missions/sentinel-1> (accessed on 3 March 2022).